An Improved Tropospheric Tomographic Model Based on Artificial Neural Network

Minghao Zhang, Kefei Zhang, Suqin Wu, Longjiang Li, Dantong Zhu, Moufeng Wan, Peng Sun, Jiaqi Shi, Shangyi Liu, and Andong Hu

***Abstract*—Global navigation satellite systems (GNSS) tropospheric tomography can be used to build a three-dimensional water vapor field. In traditional tomography, the signals crossing from the four sides of the tomographic region are not utilized. To make the best use of these valuable side-crossing signals, an improved tomographic model based on back propagation artificial neural network (BP-ANN) is proposed. In the new tomographic model, the inside part of the slant wet delay (SWD) of the side-crossing signal is divided into two sections: the isotropic and anisotropic components. The former is estimated by the zenith wet delay multiplied by the mapping function multiplied by an isotropic scale factor using a BP-ANN model, and the latter is estimated by horizontal gradients of the SWD multiplied by an anisotropic scale factor using an empirical model. The new tomographic model is experimentally evaluated using the HK CORS network measurements for the period of 21 days from 1 to 21 August 2019. Statistical results show that the root mean square error (RMSE) of slant water vapor reconstructed from the improved model is reduced to 1.35 from 2.85 mm of the traditional model. Compared with the traditional/height factor models, the percentages of the reduction in the RMSE of the tomographic result derived from the new model are 16%/9% and 22%/16%, respectively, using radiosonde and ERA5 data as references. These results suggest a good performance of the new model for GNSS tropospheric tomography.**

***Index Terms*—BP-ANN, global navigation satellite systems (GNSS), tropospheric tomography.**

I. Introduction

WATER vapor is an important parameter for both weather forecasting and climatology. Due to the advantages of high spatial-temporal resolution, all-weather conditions, low cost, nearly real-time and high accuracy of the global navigation satellite systems (GNSS) technique, water vapor retrieved from GNSS technique has been widely used in numerical weather prediction models and the research of severe weather phenomena [1], [2], [3], [4], [5]. To obtain four-dimensional (4-D) water vapor information, the tropospheric tomographic method is proposed by Flores et al. [6]. The tropospheric tomographic method has been rapidly developed during the last 20 years.

The traditional tropospheric tomography divides the tomographic region into a certain number of voxels in both horizontal and vertical domains under the assumption that the water vapor density (WVD) or wet refractivity in each voxel during the period of the GNSS tomography is constant. According to the distance of each GNSS signal travelling inside the voxels, the tomographic equation can be formed for the GNSS tomography. The tomographic observation equation matrix can be established using the slant water vapor (SWV) or slant wet delay (SWD) along the ray path of all GNSS signals during the period of the tomography. However, the shape formed from the GNSS signal ray paths during the tomographic period is similar to an inverted cone which is inconsistent with the box-shaped tomographic region. The tomographic equation matrix becomes an ill-conditioned or ill-posed problem due to the geometry of the signal distribution. To solve this problem, some iterative and non-iterative methods have been developed to resolve a tropospheric tomographic system. The singular value decomposition (SVD) is used to solve the inverse problem of a tropospheric tomographic system by Flores et al. [6], and the SVD is commonly used in noniterative methods. The damped least squares method is adopted to obtain a better tomographic result [7], and a wet refractivity Kalman filtering approach is proposed by Gradinarsky and Jarlemark [8]. Bender et al. [9] use several algebraic reconstruction techniques including algebraic reconstruction techniques, multiplicative algebraic reconstruction techniques (MART) and simultaneous iterative reconstruction technique to reconstruct a three-dimensional (3-D) wet refractivity field in Germany and the best tomographic results are obtained by using the MART. In addition, the compressive sensing method [10], and the genetic algorithm [11], are used for tropospheric tomography. For these tropospheric tomographic methods, the following three approaches including adding empirical constraint equations, introducing supplementary observations, and increasing the number of voxels crossed by GNSS

Manuscript received 29 November 2022; revised 30 March 2023 and 7 May 2023; accepted 16 May 2023. Date of publication 22 May 2023; date of current version 30 May 2023. This work was supported in part by the National Natural Science Foundation of China under Grant 42274021 and Grant 41874040, in part by the State Key Program of National Natural Science Foundation of China under Grant 41730109, in part by the Independent Innovation Project of "Double-First Class" Construction under Grant 2022ZZCX06, in part by the Programme of Introducing Talents of Discipline to Universities under Grant B20046, and in part by the 2022 Jiangsu Provincial Science and Technology Initiative-Special Fund for International Science and Technology Cooperation under Grant BZ2022018. *(Corresponding author: Kefei Zhang.)*

Minghao Zhang, Kefei Zhang, Suqin Wu, Longjiang Li, Dantong Zhu, Moufeng Wan, Peng Sun, and Shangyi Liu are with the School of Environment Science and Spatial Informatics, China University of Mining and Technology, Xuzhou 221116, China (e-mail: minghao_zhang@cumt.edu.cn; profkzhang@cumt.edu.cn; suqin_wu@cumt.edu.cn; lilongjiang@cumt.edu.cn; zdt@cumt.edu.cn; wanmoufeng@cumt.edu.cn; peng_sun@cumt.edu.cn; ts20160131p31@cumt.edu.cn).

Jiaqi Shi is with GNSS Research Center, Wuhan University, Wuhan 430079, China (e-mail: shijiaqi@whu.edu.cn).

Andong Hu is with the Cooperative Institute for Research in Environmental Sciences, University of Colorado Boulder, Boulder, CO 80309 USA (e-mail: andong.hu@colorado.edu).

Digital Object Identifier 10.1109/JSTARS.2023.3278302

signals are proposed for the regularization of the ill-conditioned tomographic system. The details of these methods are as follows.

Flores et al. [6] adopt empirical constraints including horizontal smoothing, vertical smoothing, and boundary conditions. Song et al. [12] propose a Gaussian weight function to define the weights of the horizontal constraint for all the voxels at the same height layer. In general, an exponential function is used for the vertical constraint [13]. However, it is difficult to know the real atmospheric condition in the period of the tomography, a priori information is introduced into the tomographic system. Flores et al. [6] adopt radiosonde profiles for the background field. Xia et al. [14] select radio occultation data as the a priori background field. Benevides et al. [15] analyze the impact of priori fields on the tomographic result using the prior wet refractivity profiles of atmosphere infrared sounder (AIRS) and radiosonde data.

For the second method, supplementary observations from other technologies are introduced into the tomographic system. Benevides et al. [16] and Heublein et al. [10], [17] add observations from interferometric synthetic aperture radar (InSAR) data into the tropospheric tomographic system. Benevides et al. [18] and Zhang et al. [19], [20] use water vapor products from moderate-resolution imaging spectroradiometer as supplementary observations for the GNSS tropospheric tomographic system. Zhang et al. [21] add water vapor products of the Fengyun-4A satellite into the GNSS tropospheric tomographic system. Chen and Liu [22] introduce water vapor observations from radiometers and sun photometers into the tropospheric tomographic system. Since the temporal/spatial resolutions of these observations are much lower than GNSS data, the number of the observations which can be added to the GNSS tomographic system is limited. In the traditional tomographic model, the GNSS signals crossing from the top boundary of the tomographic region are used, whilst the signals crossing from the side faces of the tomographic region are discarded. Therefore, recent studies tend to make the best use of the side-crossing signals and multi-GNSS signals in tropospheric tomography. Benevides et al. [23] and Dong et al. [24] utilize multi-GNSS observations to reduce the number of empty voxels. Rohm and Bosy [25] propose a method that used the University of New Brunswick version 3 modified model to obtain the SWD of the side-crossing signals inside the tomographic region. Benevides et al. [18] adopt an exponential law to represent the diminishing of the wet refractivity along the vertical direction and estimate the SWD inside the tomographic region for the side-crossing signals. Yao and Zhao [26] develop a water vapor unit index model based on both radiosonde data and the GNSS signals crossing from the top boundary of the tomographic region to estimate the initial WVD constraint for every height layer. Zhao et al. [27] develop an exponential height factor model to account for the side-crossing signals by expanding the tomographic region in the horizontal domain. Zhao et al. [28] improve this exponential model based on the Global Pressure and Temperature 2 wet model. By dividing the SWD into two parts—isotropic and anisotropic components, Zhang et al. [29] construct a height factor model (HFM) based on 30-year radiosonde data. In addition, Chen and Liu [30] and Yao and Zhao [31] use the optimal voxel distribution method to increase the number of voxels crossed by signals.

Water vapor varies highly in the spatial and temporal domains. However, in all the approaches using side-crossing signals mentioned above, the spatiotemporal characteristics of water vapor are not considered. In this study, the spatiotemporal characteristics are considered to develop the new tomographic model using the top-crossing and side-crossing signals. For the improved tomographic model, ERA5 hourly ($0.125° \times 0.125°$) grid data are used to construct an improved isotropic scale factor model. The isotropic components of the SWD of side-crossing signals inside the tomographic region are estimated using the improved isotropic scale factor model. More specifically, the parameters of the isotropic scale factor model include not only the height, which is the only factor considered in the HFM but also the information of the spatiotemporal characteristics of the water vapor and the zenith wet delay (ZWD) at the GNSS station. In addition, the anisotropic component of the SWD of side-crossing signals inside the tomographic region is estimated by the experiential model. For the improved tomographic model, the SWD of the side-crossing signals inside the tomographic region is added into the tomographic system. Moreover, three tomographic schemes are designed for the performance evaluation of the improved tomographic model, and both radiosonde data and ERA5 grid data are selected as the two references.

The rest of this article is organized as follows. In Section II, the data and methods are introduced. Section III describes the new tomographic model using top-crossed and side-crossed GNSS signals. The validation of the new tomographic model is presented and analyzed in Section IV. Finally, Section V concludes this artice.

II. Data and Methods

In this study, the following three types of data from the Hong Kong region are used.

1) GNSS data from the Hong Kong Satellite Positioning Reference Station Network.
2) Radiosonde data collected at the King's Park meteorological station.
3) ERA5 reanalysis grid data from the European Centre for Medium-Range Weather Forecast (ECMWF).

The GNSS data are used to establish the tomographic equations. The radiosonde data are used to evaluate the results of the new tomographic model. The ERA5 reanalysis grid data are used to develop the isotropic scale factor model and validate the results of the new tomographic model. The methodology of GNSS tropospheric tomography and the artificial neural network used in this study are elaborated.

A. Data

1) GNSS Data: In this study, GNSS data with a 30 s sampling rate from 16 CORS stations in Hong Kong and three International GNSS Service (IGS) stations (BJFS, JGFN, and PIMO) during the 21 days from 1 to 21 August 2019 are selected for the tomographic experiment. The main reason for this selection is that this period contained sunny days, rainy days, and the value of water vapor is larger. In the GNSS data processing, the SWD

is expressed as follows:

$$\text{SWD} = \overbrace{mf_w(\varepsilon)\ \text{ZWD}}^{\text{Isotropic component}} + \underbrace{mf_g(\varepsilon)\ \left(G^w_{NS}\cos(\alpha) + G^w_{EW}\sin(\alpha)\right)}_{\text{Anisotropic component}} \quad (1)$$

where ZWD is the zenith wet delay estimated by the GNSS at MIT (GAMIT) / Global Kalman filter (GLOBK) software package [32], $mf_w(\varepsilon)$ and $mf_g(\varepsilon)$ are the mapping functions for the wet delay and gradients components, respectively, G^w_{NS} and G^w_{EW} are the horizontal gradients in the north-south and east-west directions, respectively, and ε, α are the elevation and azimuth angles of the signal path from the GNSS data processing, respectively. Since the SWV is used for tropospheric tomography in this study, the SWD retrieved from the GNSS signal needs to be transformed into the SWV by the following formula:

$$\text{SWV} = \frac{10^6}{R_V\left(\frac{k_3}{T_m} + k'_2\right)}\text{SWD} \quad (2)$$

where k'_2, k_3, and R_V are the specific gas constants [33]. T_m is the weighted mean temperature which can be calculated by an empirical model from Liu et al. [34].

2) Radiosonde Data: In this article, the 21 years (2000–2020) sounding data (twice per day), which are acquired from the Integrated Global Radiosonde Archive [35], are used at King's Park meteorological station. The used parameters of radiosonde data include the observations of temperature, pressure, water vapor pressure, and geopotential height at different pressure layers. The data are used to estimate the ZWD and WVD at the radiosonde station by the formulations [36], [37]

$$\text{ZWD} = \sum_{h_s}^{h_t}\left(k'_2\frac{P_w}{T} + k_3\frac{P_w}{T^2}\right)dh \quad (3)$$

where h_s and h_t are the heights of the bottom and top pressure layers, respectively, P_w and T are the water vapor pressure (hPa) and temperature (K), respectively, and k'_2 and k_3 are the ideal gas constants from Thayer [33]

$$\rho_0 = \frac{P_w}{R_v T} \quad (4)$$

where ρ_0 is the WVD, P_w and T are the water vapor pressure (hPa) and temperature (K), respectively, and R_v is the specific gas constant for water vapor.

3) ERA5 Data: ERA5 is the latest reanalysis data product from ECMWF and provides meteorological data at 37 pressure layers from 1000 to 1 hPa, such as pressure, temperature, geopotential height, and specific humidity. The ERA5 hourly 0.125° × 0.125°grid data in the region of Hong Kong are used to calculate the ZWD in (3) and WVD in (4). The 9-years (2011–2019) ERA5 grid data [38] are used to construct the isotropic scale factor model contained in the improved tomographic model. The ERA5 grid data are also used to evaluate the isotropic scale factor model and the result of the tomography.

B. GNSS Tropospheric Tomography

The tropospheric tomographic region is divided into a certain number of voxels. The SWV of a GNSS signal ray inside the tomographic region can be calculated by the WVD multiplied by the distance of the signal ray path inside the voxels crossed by the signal [6]

$$\text{SWV} = \sum_{i,j,k}^{n}\rho_{i,j,k}d_{i,j,k} \quad (5)$$

where SWV (mm) is the slant water vapor along the signal, *i*, *j*, *k* are the indices of the voxel in the longitude, latitude, and vertical domains, respectively, $\rho_{i,j,k}$ (g/m^3) and $d_{i,j,k}$ (km) denote the WVD and distance in the voxel (*i*, *j*, *k*) passed by the ray, respectively, and n is the number of all the voxels crossed by the ray.

The observation equation system for all SWVs contained in the tomographic region can be expressed in the matrix form as follows:

$$\boldsymbol{SWV_{top}} = \boldsymbol{A_{top}X} \quad (6)$$

where $\boldsymbol{SWV_{top}}$ includes the SWVs of the GNSS signals crossing from the top boundary of the tomographic region, $\boldsymbol{A_{top}}$ is the coefficient matrix including the length of the top-crossing signals crossing through each voxel, and $\boldsymbol{X}$ is the column vector including the unknown WVD parameters in all voxels.

To obtain a better tomographic result, horizontal and vertical constraint equations are applied. The horizontal constraint for each height layer is a weighted mean WVD of all the voxels at the layer [6]

$$w_{1,1,k}\,\rho_{1,1,k} + \ldots + w_{i-1,j-1,k}\,\rho_{i-1,j-1,k} + \ldots - \rho_{i,j,k} + \ldots + w_{i+1,j+1,k}\,\rho_{i+1,j+1,k} + \ldots = 0 \quad (7)$$

where $w_{1,1,k}, w_{i-1,j-1,k}\ldots$ denote the weight coefficient of each voxel at the k height layer. $\rho_{1,1,k,}, \rho_{i-1,j-1,k}\ldots$ denote the WVD of each voxel. i, j, and k are the indices of the voxel in the longitude, latitude, and vertical domain.

The weight of a voxel is estimated using the Gauss weighting function [12]:

$$w^{il,jl,k}_{i,j,k} = -\frac{e^{-\frac{d^2_{il,jl,k}}{2\sigma^2}}}{\sum_{il=1}^{ne}\sum_{jl=1}^{nn}e^{-\frac{d^2_{il,jl,k}}{2\sigma^2}}} \quad (8)$$

Where i, j, and k are the indices of the target voxel in the three spatial dimensions, il, jl, and k are that of the other voxels at the same height layer, $d_{il,jl,k}$ is the distance between the target voxel and the other voxels, σ is the smoothing factor, and ne and nn are the numbers of voxels in the longitude and latitude domains, respectively.

According to previous research [13], WVD usually decreases with height, and the variation trend is close to the exponential function. As a result, the exponential function is selected as the vertical constraint for the relationship between the WVDs of two vertical adjacent voxels with indices i, j, k and $i, j, k+1$

$$\rho_{i,j,k+1} = e^{-\frac{h_{i,j,k+1}-h_{i,j,k}}{\text{SH}}}\rho_{i,j,k} \quad (9)$$

where ρ (g/m^3) denotes the WVD, h (km) is the height of the vertical layer, SH is the scale height of the water vapor, for which a 2 km value is selected in this study, and i, j, k and $i, j, k+1$ are the indices of two adjacent voxels in the vertical domain.

As we all know, the error in the SWV increases with the reduction in the elevation angle of the signal ray path. Hence, a function that expresses such a relationship is adopted for the weight of the observation equation matrix. The identity matrices are adopted for the weight of the horizontal and vertical constraints [17], [29].

The tomographic observation equation matrix is as follows:

$$\begin{pmatrix} \boldsymbol{P_{top}SWV_{top}} \\ 0 \\ 0 \end{pmatrix} = \begin{pmatrix} \boldsymbol{P_{top}A_{top}} \\ \boldsymbol{P_{hr}H} \\ \boldsymbol{P_{vr}V} \end{pmatrix} \boldsymbol{X} \tag{10}$$

where $\boldsymbol{SWV_{top}}$ denotes the observation vector from the top-crossing signals, $\boldsymbol{A_{top}}$ is the observation matrix of top-crossing signals, $\boldsymbol{H}$ and $\boldsymbol{V}$ are the horizontal and vertical constraint matrices, respectively, $\boldsymbol{P_{top}}, \boldsymbol{P_{hr}}, \boldsymbol{P_{vr}}$ denote the weight matrices of observation equations for top-crossing signals, horizontal and vertical constraints, respectively, and $\boldsymbol{X}$ denotes the vector of the unknown WVD parameters of all voxels in the tomographic region.

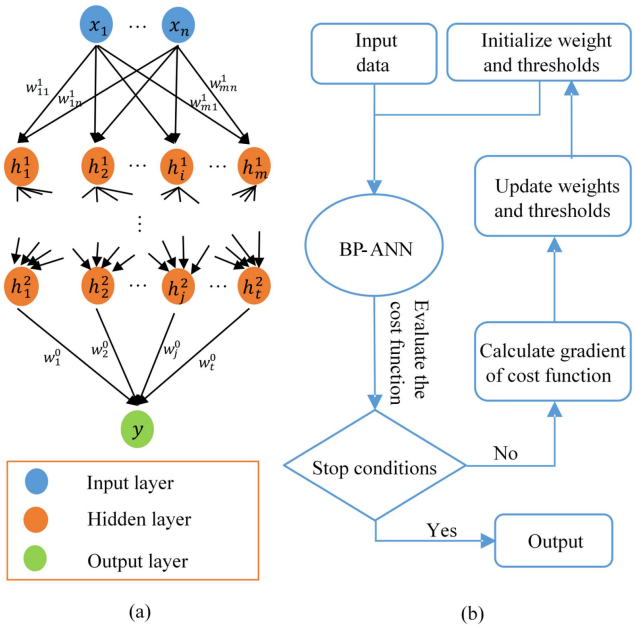

Fig. 1. (a) Structure of an ANN system. (b) Flowchart and steps of training BP-ANN.

C. BP-ANN

In previous studies, the feed-forward BP neural network (BP-NN) technique has been popularly applied in various geoscientific research [39], [40], [41], since it can solve non-linear problems with different structures and precisions. A BP-NN model is composed of one input layer, one or more hidden layers, and one output layer, and each layer contains at least one neuron. The training of the BP-NN has two processes including the forward propagation of input parameters and the backpropagation of the "loss" value. The forward propagation of input parameters is used to obtain predicted values. The backpropagation of the "loss" value which is the error of desired outputs [42] is used to update the weight matrix and offset vector. The forward propagation of input parameters can be simply expressed as follows:

$$\boldsymbol{Y_{bp}} = f_2\left(\boldsymbol{w_2^{bp}} f_1\left(\boldsymbol{w_1^{bp}X_{bp}} + \boldsymbol{a_1^{bp}}\right) + \boldsymbol{a_2^{bp}}\right) \tag{11}$$

where $\boldsymbol{X_{bp}}$ and $\boldsymbol{Y_{bp}}$ are the input and predicted vectors, respectively, $\boldsymbol{w_1^{bp}}$ and $\boldsymbol{a_1^{bp}}$ are the weight matrix and offset vector between the input layer neurons and hidden layer neurons, respectively, $\boldsymbol{w_2^{bp}}$ and $\boldsymbol{a_2^{bp}}$ are the weight matrix and offset vector between the hidden layer neurons and output layer neurons, respectively, and f_1 and f_2 are two activation functions.

The purpose of the backpropagation is to update the weight matrix and offset vector for the forward propagation using the error between the desired value and the predicted result

$$\boldsymbol{w_{m+1}^{bp}} = \boldsymbol{w_m^{bp}} - \eta J'_w\left(\boldsymbol{w_m^{bp}}, \boldsymbol{a_m^{bp}}\right) \tag{12}$$

$$\boldsymbol{a_{m+1}^{bp}} = \boldsymbol{a_m^{bp}} - \eta J'_a\left(\boldsymbol{w_m^{bp}}, \boldsymbol{a_m^{bp}}\right) \tag{13}$$

where $\boldsymbol{w_{m+1}^{bp}}$ and $\boldsymbol{a_{m+1}^{bp}}$ are the weight matrix and offset vector of the m+1 th iterative result, $\boldsymbol{w_m^{bp}}$ and $\boldsymbol{a_m^{bp}}$ are the weight matrix and offset vector of the m th iterative result. m and m+1 are the iterations, η is the learning rate, and $J'_w(\boldsymbol{w_m^{bp}}, \boldsymbol{a_m^{bp}})$ and $J'_a(\boldsymbol{w_m^{bp}}, \boldsymbol{a_m^{bp}})$ are the partial derivatives of the cost function which is constructed by the aforementioned error. The structure of a BP-ANN model and the flowchart of training the BP-ANN model are shown in Fig. 1.

D. Validation Method

To evaluate the accuracy of the isotropic scale factor from the new model, three error evaluation indicators, including bias, root mean square error (RMSE), and standard deviation (STD) are used. The accuracy of WVD from the new tomographic model is evaluated using three error evaluation indicators including bias, RMSE, and mean absolute error (Mae)

$$\text{bias} = \frac{\sum(y - y')}{N} \tag{14}$$

$$\text{RMSE} = \sqrt{\frac{\sum(y - y')^2}{N}} \tag{15}$$

$$\text{STD} = \sqrt{\frac{\sum(y - y' - \mu)^2}{N}} \tag{16}$$

$$\text{Mae} = \frac{\sum(|y - y'|)}{N} \tag{17}$$

where N is the number of samples, y and y' are the isotropic scale factor / WVD from the tomographic model and validation data from radiosonde and ERA5 data, respectively, and μ is the mean value of the differences between two datasets.

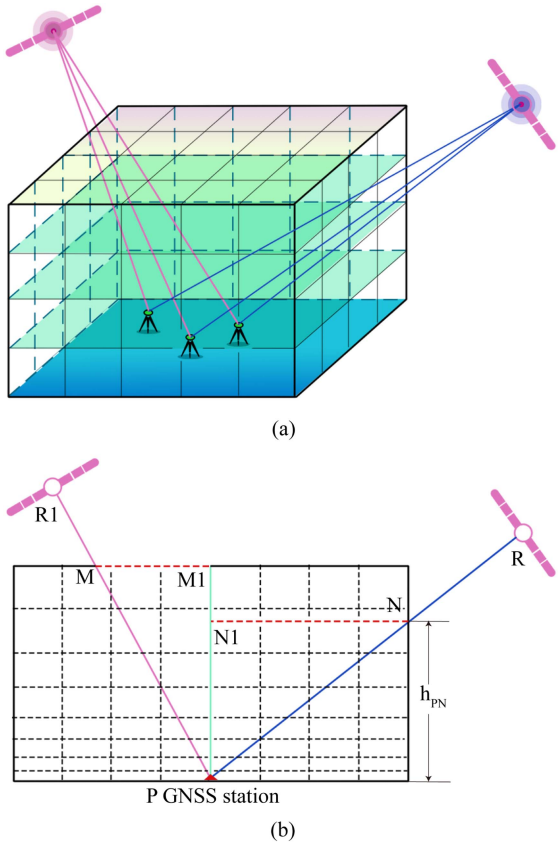

Fig. 2. (a) Three-dimensional view and (b) side-view of top-crossing (purple) and side-crossing (blue) signals used in GNSS tropospheric tomography. (b) Illustrates the vertical intersection of the two types of signals. MM1 denotes the top layer of the tomographic region, i.e., the top of the tropopause. PM1 (green vertical line) is the height of the tropopause at the GNSS station. h_{PN} is the height of the side-crossing signal (PR) crossing from the tomographic region.

III. New Tomographic Model Based on BP Neural Network

In the traditional tropospheric tomographic model, only those signals that pass from the top boundary of the tomographic region are utilized. The signals that cross from the side faces of the tomographic region are ignored, which leads to a "waste" of these signals and a decrease in the number of voxels penetrated by these signals. In this study, a new method which improves the use of side-crossing signals is developed for tropospheric tomography. In Fig. 2(a), the 3-D view of the top-crossing and side-crossing signals is represented.

In the observation equation of GNSS data processing, the slant tropospheric delay can be expressed as a function of the zenith total delay (ZTD), and the ZTD is estimated from GNSS data processing. The ZWD can be calculated by the ZTD minus the zenith hydrostatic delay (ZHD) which can be obtained using the Saastamoinen model. The SWD can be obtained by the ZWD multiplied by a mapping function (the isotropic component) and horizontal gradients (the anisotropic component). In Fig. 2(b), the SWD of a side-crossing signal (PN), which is a part of the signal (PR) inside the tomographic region, can be expressed by its wet delay in the zenith direction (ZWD from P to N1) multiplied by a mapping function (the isotropic component) and its horizontal gradients (the anisotropic component). In this study, an isotropic scale factor model and an anisotropic scale factor model are developed to estimate the isotropic and anisotropic scale factors, respectively. The two scale factors are the ratio of the part of the signal inside the tomographic region to the whole signal for the isotropic and anisotropic components, respectively. Therefore, the SWD of a side-crossing signal inside the tomographic region can be expressed by the isotropic scale factor multiplied by the isotropic component plus the anisotropic scale factor multiplied by the anisotropic component. The procedure of the scale factor models is detailed in Section III-A and B. The tomographic equations of the new tomographic model are shown in Section III-C.

A. Isotropic Component of SWD From Side-Crossing Signals

The isotropic component of an SWD is obtained by the ZWD multiplied by a mapping function. The isotropic component of the SWD of a side-crossing signal inside the tomographic region can be obtained by the isotropic scale factor multiplied by the ZWD multiplied by the mapping function. The main idea of the isotropic scale factor model is as follows. The side-crossing signal (RP) in Fig. 2(b) is used as an example to show the process of developing the isotropic component model.

1) Obtaining the isotropic component of the SWD for the whole signal.

In Fig. 2(b), the RP is a whole signal path and h_{PM1} (green vertical line) is the height of the tropopause at the GNSS station P. The isotropic part of a SWD and the zenith wet delay for the whole signal path (RP) can be expressed as follows:

$$\mathrm{SWD}(RP)_{\mathrm{iso}} = \mathrm{ZWD}_{\mathrm{total}}\, mf_w(\varepsilon) \tag{18}$$

$$\mathrm{ZWD}_{\mathrm{total}} = \int_{h_P}^{h_{M1}} N_w dh \tag{19}$$

where $\mathrm{ZWD}_{\mathrm{total}}$ is the whole zenith wet delay at GNSS station P, RP is the signal path, h_P and h_{M1} are the height of the GNSS site and the top of the tomographic model, respectively, N_w is the wet refractivity, $\mathrm{SWD}(RP)_{\mathrm{iso}}$ is the isotropic part of the SWD of the signal (RP), $mf_w(\varepsilon)$ is the wet mapping function, and ε is the elevation angle of the signal (RP).

2) Obtaining the isotropic component of the SWD for the signal inside the tomographic region.

The signal (PN) is a segment of the path of the signal (RP), and the wet delay of the signal (PN) can be expressed by the ZWD which is the integral of the wet refractivity from h_P to h_{N1} (h_{N1} is the height of signal (RP) crossing from the side face of the tomographic model) multiplied by a mapping function. The two equations are as follows:

$$\mathrm{SWD(PN)}_{\mathrm{iso}} = \mathrm{ZWD}_{h_{PN1}}\, mf_w(\varepsilon) \tag{20}$$

$$\mathrm{ZWD}_{h_{PN1}} = \int_{h_P}^{h_{N1}} N_w dh \tag{21}$$

where $\mathrm{ZWD}_{h_{PN1}}$ is the partial ZWD, h_P and h_{N1} are the height of the GNSS site and the signal crossing from the tomographic model, respectively, $\mathrm{SWD(PN)}_{\mathrm{iso}}$ is the isotropic part of the SWD of signal (RP) inside the tomographic model, i.e., the SWD of signal path (PN).

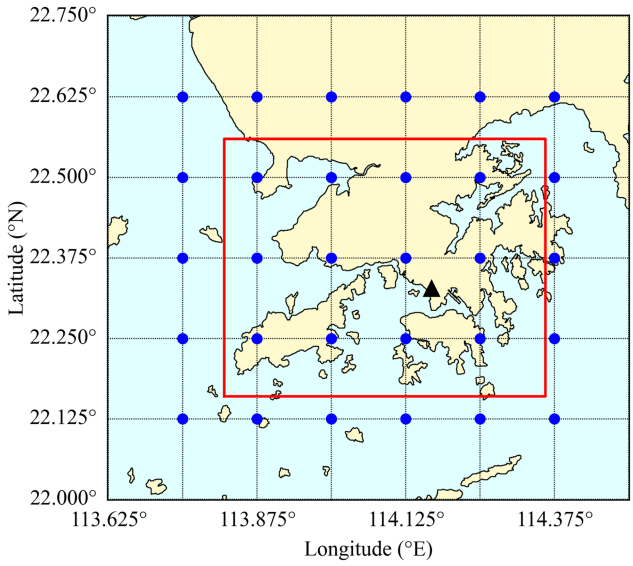

Fig. 3. ERA5 grid points are used to construct the isotropic scale factor model. The blue dots are ERA5 grid points, and the red rectangle is the tomographic region.

3) Defining isotropic scale factor.

According to (18) and (20), the isotropic scale factor of the side-crossing signal can be expressed as follows:

$$\lambda_{\text{iso}}\left(h_{\text{PN1}}\right) = \frac{\text{SWD(PN)}_{\text{iso}}}{\text{SWD(RP)}_{\text{iso}}} = \frac{\text{ZWD}_{h_{\text{PN1}}}}{\text{ZWD}_{\text{total}}} \tag{22}$$

where $\lambda_{\text{iso}}(h_{\text{PN1}})$ is the isotropic scale factor of the station *P* at the height h_{PN1}.

Therefore, $\text{SWD(PN)}_{\text{iso}}$ can be expressed as follows:

$$\text{SWD(PN)}_{\text{iso}} = \lambda_{\text{iso}}\left(h_{\text{PN1}}\right)\ \text{ZWD}_{\text{total}}\ mf_w\left(\varepsilon\right) \tag{23}$$

where $\text{SWD(PN)}_{\text{iso}}$ is the isotropic part of the SWD of the signal (RP) inside the tomographic model, i.e., the SWD of signal path (PN), λ_{iso} is the isotropic scale factor at the height h_{PN1} and $mf_w(\varepsilon)$ is the mapping function, ε is the elevation angle of the signal (RP), and $\text{ZWD}_{\text{total}}$ is the whole zenith wet delay at GNSS station P.

According to (22), the isotropic scale factor general form is as follows:

$$\lambda_{\text{iso}}\left(h\right) = \frac{\text{ZWD}_h}{\text{ZWD}_{\text{total}}} \tag{24}$$

where $\lambda_{\text{iso}}(h)$ is the isotropic scale factor at the height *h*, ZWD_h and $\text{ZWD}_{\text{total}}$ are the partial ZWD inside the tomographic region and the whole ZWD at the station, respectively, and *h* is the height of the signal crossing from the tomographic model.

4) Calculating isotropic scale factor using ERA5 data.

In this research, ERA5 hourly grid data (with the horizontal resolution of 0.125 × 0.125°) in Hong Kong during the period from 2011 to 2019 are used to construct the regional isotropic scale factor model. The grid points used to develop the model are shown in Fig. 3.

To develop the isotropic scale factor model, ZWD_h and $\text{ZWD}_{\text{total}}$ in (24) need to be calculated using ERA5 data with (19), (21), and (3)

$$\text{ZWD}_{\text{total}} = \int_{h_s}^{h_{\text{TRP}}} N_w dh \approx \sum_{h_s}^{h_{\text{TRP}}} \left(k_2^{'}\frac{P_w}{T} + k_3\frac{P_w}{T^2}\right)\Delta h \tag{25}$$

$$\text{ZWD}_{h_l} = \int_{h_S}^{h_l} N_w dh \approx \sum_{h_s}^{h_l} \left(k_2^{'}\frac{P_w}{T} + k_3\frac{P_w}{T^2}\right)\Delta h \tag{26}$$

where $\text{ZWD}_{\text{total}}$ and ZWD_{h_l} are the whole ZWD and partial ZWD from h_S to h_l at the grid point. h_S, h_{TRP}, and h_l are the height of the lowest pressure layer of the ERA5 grid point, the height of the tropopause at the grid point, and the height of the other pressure layers of the ERA5 grid point.

Then, the isotropic scale factors ($\lambda_{\text{iso}}(h)$) of each grid point in the height of each pressure layer (under the height of the tropopause) can be calculated. These isotropic scale factors are used to develop the isotropic scale factor model.

5) Developing the isotropic scale factor model using BP-ANN.

In the previous study, the exponential function is adopted to fit the scale factor model. However, the exponential model, like any fitting model, only reflects the general variation trend of $\lambda_{\text{iso}}(h)$ with low temporal and spatial resolutions. To construct a refined isotropic scale factor model, the BP-ANN is applied in this study.

Fig. 4 shows the structure of the input layer, hidden layers, and output layer for the new isotropic scale factor model. For this model, the isotropic scale factor ($\lambda_{\text{iso}}(h)$) is set as output variables, and seven variables including year, day of year (doy), hour of day (HoD), latitude, longitude, height (the height of the pressure layer), and the whole ZWD are set as the input variables. In this study, the isotropic scale factors from step 4) are used as the output data and the seven variables of each scale factor make up the input data. The input and output data are used to train the BP-ANN model. In the training process of the BP-ANN model, the Levenberg Marquardt algorithm is used to update the weight matrices. The ratios of the training, validation, and test datasets are 70%, 15%, and 15%, respectively. The threshold for error precision of the training process is set to 0.001. At present, some experimental equations are used to calculate the number of nodes of the hidden layer, but this value only is a reference value. To construct a better model, many schemes are tested for identifying the optimal number of nodes in the hidden layer, the optimal number of the hidden layers, and the optimal active functions. Finally, the structure with 7, 4, and 2, combined with the active functions of the logsig for the three hidden layers of the BP-ANN are determined.

6) Obtaining λ_{iso} of GNSS site using the new model

In a tropospheric tomography, information of time (year, doy, HoD), location of the GNSS station (longitude, latitude, and height of side-crossing signal crossing from the tomographic model) and the whole ZWD of each GNSS site can be obtained as the input value of the new isotropic scale factor model. Then, the output value of the new scale factor model, i.e., the λ_{iso} of each side-crossing signal can be obtained. According to (23), the isotropic component of the SWD of the side-crossing signal

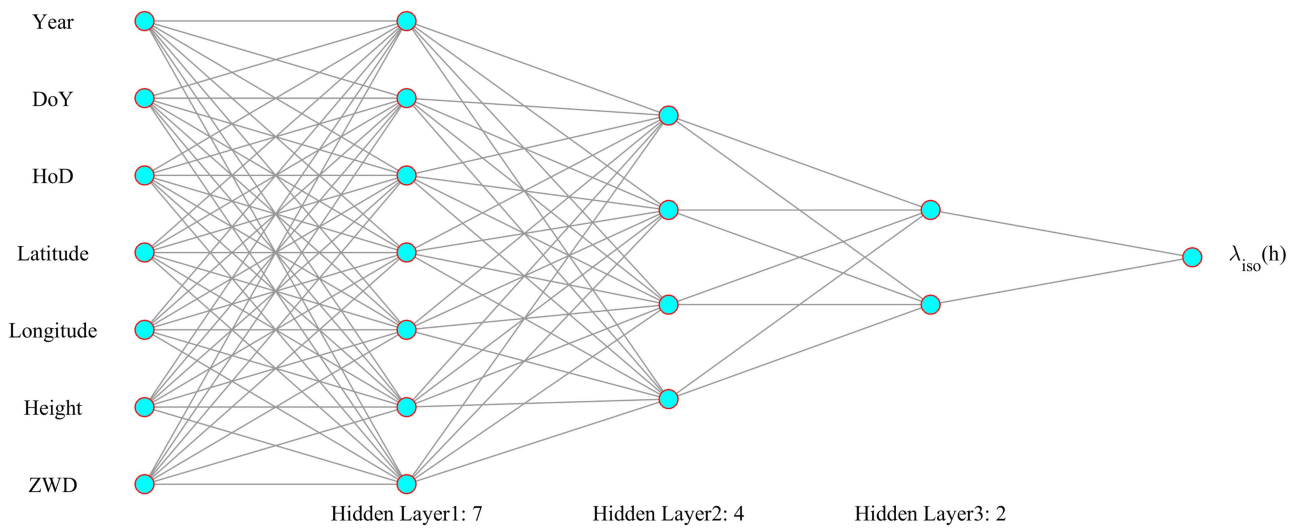

Fig. 4. Structure of the BP neural network.

can be expressed

$$\mathrm{SWD}(h)_{\mathrm{iso}} = \lambda_{\mathrm{iso}}(h)\ \mathrm{ZWD}_{\mathrm{total}}\, mf_w(\varepsilon) \tag{27}$$

where $\mathrm{SWD}(h)_{\mathrm{iso}}$ is the SWD of the side-crossing signal path under the height h, $\lambda_{\mathrm{iso}}(h)$ is the isotropic scale factor of the GNSS site at the height h, $mf_w(\varepsilon)$ is the mapping function of wet delay, ε is the elevation angle of the signal path, and h is the height of the side-crossing signal crossing from the tomographic region.

B. Anisotropic Component of SWD From Side-Crossing Signals

The horizontal gradients of the wet delay are another part of a SWD, and numerous studies have investigated the characteristic of the horizontal gradients using very long baseline interferometry [43], [44]. The horizontal gradient of the β direction can be expressed as the integral of the wet refractivity gradient with height

$$G_\beta = 10^{-6} \int N_\beta(h)\, hdh \tag{28}$$

where G_β is the azimuthal asymmetry of the atmosphere, i.e., the horizontal gradient in the β direction, $N_\beta(h)$ is the wet refractivity gradient at height h, and β is the azimuth direction including north-south and east-west directions.

Since it is difficult to directly obtain $N_\beta(h)$ in a tomographic modelling process, it is assumed that the refractive gradient varies exponentially with height in this study, as the work of Zhang et al. [29]

$$N_\beta(h) = e^{-\frac{h}{\mathrm{SH}}}\ N_\beta^S \tag{29}$$

where $N_\beta(h)$ is the wet refractive gradient of the β direction at the height h, N_β^S is the wet refractive gradient of the β direction at the surface of the site, β is the azimuth directions including north-south and east-west directions, SH is the scale height of water vapor (1–2 km).

Substituting (29) into (28) leads to the following:

$$G_\beta = 10^{-6} \int e^{-\frac{h}{\mathrm{SH}}} N_\beta^S hdh \tag{30}$$

where G_β is the azimuthal asymmetry of the atmosphere, i.e., horizontal gradient, N_β^S is the wet refractive gradient of the β direction at the surface of the site, β is the azimuth directions including north-south and east-west directions, and SH is the scale height of water vapor.

Equation (30) can be expressed by partial integral calculus

$$G_\beta = 10^{-6} N_\beta^S \left[-Hhe^{-\frac{h}{\mathrm{SH}}} + \mathrm{SH} \int e^{-\frac{h}{\mathrm{SH}}} dh\right]. \tag{31}$$

Therefore, horizontal gradient (anisotropic component) can be obtained

$$G_\beta^{h_{\mathrm{top}}} = 10^{-6} N_\beta^S \left[\left(-\mathrm{SH}he^{-\frac{h}{\mathrm{SH}}} - \mathrm{SH}^2 e^{-\frac{h}{\mathrm{SH}}}\right)\Big|_0^{h_{\mathrm{top}}}\right] \tag{32}$$

$$G_\beta^{h_{\mathrm{top}}} = 10^{-6} N_\beta^S \left[\mathrm{SH}^2 + e^{-\frac{h_{\mathrm{top}}}{\mathrm{SH}}}\left(-\mathrm{SH}^2 - h_{\mathrm{top}}\mathrm{SH}\right)\right]. \tag{33}$$

Replacing h_{top} with h leads to the following:

$$G_\beta^h = 10^{-6} N_\beta^S \left[\mathrm{SH}^2 + e^{-\frac{h}{\mathrm{SH}}}\left(-\mathrm{SH}^2 - h\mathrm{SH}\right)\right] \tag{34}$$

where $G_\beta^{h_{\mathrm{top}}}$ is the whole horizontal gradient at the β direction, G_β^h is the partial horizontal gradient of the β direction at the height h, β is the azimuth directions including north-south and east-west directions, and h_{top} and h are the height of the tropopause and side-signal crossing from the tomographic model, respectively.

The main idea of the anisotropic scale factor model is as follows. The side-crossing signal (PR) in Fig. 2(b) is used as an example to show the process of developing the anisotropic component model. According to the anisotropic component term, i.e., the last term in (1), the anisotropic component of the signal (PR) can be expressed

$$\mathrm{SWD}(\mathrm{PR})_{\mathrm{aniso}} = mf_g(\varepsilon)\left(G_{\mathrm{NS}}^{h_{PM}}\cos(\alpha) + G_{\mathrm{EW}}^{h_{PM}}\sin(\alpha)\right) \tag{35}$$

where $\mathrm{SWD(PR)}_{\mathrm{aniso}}$ is the anisotropic component of the SWD for the signal (PR), $G_{\mathrm{NS}}^{h_{PM}}$ and $G_{\mathrm{EW}}^{h_{PM}}$ are whole horizontal gradient components in north-south and east-west directions which are calculated by (33), h_{PM} is the height of the tropopause, $mf_g(\varepsilon)$ is the mapping function of the horizontal gradient components, and ε, α are the elevation and azimuth angle of the signal (PR), respectively.

Similarly, for the part of the side-crossing signal (PR) that is within the tomographic region, i.e., PN in Fig. 2(b), its anisotropic component can be expressed as follows:

$$\mathrm{SWD(PN)}_{\mathrm{aniso}} = mf_g(\varepsilon)\left(G_{\mathrm{NS}}^{h_{\mathrm{PN}}}\cos(\alpha) + G_{\mathrm{EW}}^{h_{\mathrm{PN}}}\sin(\alpha)\right) \tag{36}$$

where $G_{\mathrm{NS}}^{h_{\mathrm{PN}}}$ and $G_{\mathrm{EW}}^{h_{\mathrm{PN}}}$ are the north-south and east-west horizontal gradient components of the signal (PR) within the tomographic region, i.e., the north-south and east-west horizontal gradient components from the ground up to the height h_{PN}, and they can be obtained from (34), h_{PN} is the height of the side-crossing point of the signal (PR), $mf_g(\varepsilon)$ is the mapping function of the horizontal gradient components, and ε, α are the elevation and azimuth angle of the signal (PN), respectively.

Substituting (33) and (34) into (35) and (36), respectively, the anisotropic scale factor becomes as follows:

$$\begin{aligned}\lambda_{\mathrm{aniso}}(h_{\mathrm{PN}}) &= \frac{\mathrm{SWD(PN)}_{\mathrm{aniso}}}{\mathrm{SWD(PR)}_{\mathrm{aniso}}} \\ &= \frac{\mathrm{SH}^2 + e^{-\frac{h_{\mathrm{PN}}}{\mathrm{SH}}}\left(-\mathrm{SH}^2 - h_{\mathrm{PN}}\mathrm{SH}\right)}{\mathrm{SH}^2 + e^{-\frac{h_{\mathrm{top}}}{\mathrm{SH}}}\left(-\mathrm{SH}^2 - h_{\mathrm{top}}\mathrm{SH}\right)}.\end{aligned} \tag{37}$$

The general form of (37) can be expressed by replacing h_{PN} with h

$$\lambda_{\mathrm{aniso}}(h) = \frac{\mathrm{SH}^2 + e^{-\frac{h}{\mathrm{SH}}}\left(-\mathrm{SH}^2 - h\ \mathrm{SH}\right)}{\mathrm{SH}^2 + e^{-\frac{h_{\mathrm{top}}}{\mathrm{SH}}}\left(-\mathrm{SH}^2 - h_{\mathrm{top}}\ \mathrm{SH}\right)} \tag{38}$$

where $\lambda_{\mathrm{aniso}}(h)$ is the anisotropic scale factor, h is the height of the point from which the side-crossing signal crosses the tomographic region, h_{top} is the height of the tropopause, which is also the same as the top of the tomographic region, and SH is the scale height of water vapor.

Considering (35) and (37), the anisotropic component of the signal (PN) shown in Fig. 2(b) can be expressed as follows:

$$\begin{aligned}&\mathrm{SWD(PN)}_{\mathrm{aniso}} \\ &\quad= \lambda_{\mathrm{aniso}}(h_{\mathrm{PN}})\ \mathrm{SWD(PR)}_{\mathrm{aniso}} \\ &\quad= \lambda_{\mathrm{aniso}}(h_{\mathrm{PN}})\ mf_g(\varepsilon)\left(G_{\mathrm{NS}}^{h_{\mathrm{top}}}\cos(\alpha) + G_{\mathrm{EW}}^{h_{\mathrm{top}}}\sin(\alpha)\right)\end{aligned} \tag{39}$$

where $\mathrm{SWD(PN)}_{\mathrm{aniso}}$ and $\mathrm{SWD(PR)}_{\mathrm{aniso}}$ are the anisotropic components of SWDs from the signal (PN) and signal (PR). $\lambda_{\mathrm{aniso}}(h_{\mathrm{PN}})$ is the anisotropic scale factor at the height h_{PN}, $G_{\mathrm{NS}}^{h_{\mathrm{top}}}$ and $G_{\mathrm{EW}}^{h_{\mathrm{top}}}$ are whole horizontal gradient components in north-south and east-west directions, h_{top} is the height of the tropopause, which is also the same as the top of the tomographic region. h_{PN} is the height of the signal (PR) crossing from the tomographic region, $mf_g(\varepsilon)$ is the mapping function of the horizontal gradient components, and ε, α are the elevation and azimuth angle of the signal (PR), respectively.

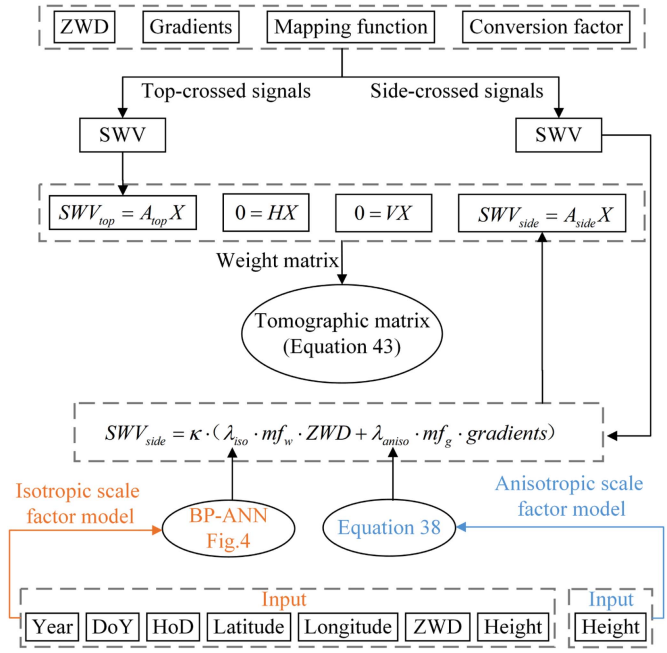

Fig. 5. Flowchart of the new tropospheric tomographic model.

Therefore, for any side-crossing signal, the anisotropic component of the SWD of the side-crossing signal inside the tomographic region can be obtained

$$\begin{aligned}\mathrm{SWD}(h)_{\mathrm{aniso}} &= \lambda_{\mathrm{aniso}}(h)\ \mathrm{SWD}(h_{\mathrm{top}})_{\mathrm{aniso}} \\ &\lambda_{\mathrm{aniso}}(h)\ mf_g(\varepsilon)\left(G_{\mathrm{NS}}^{h_{\mathrm{top}}}\cos(\alpha) + G_{\mathrm{EW}}^{h_{\mathrm{top}}}\sin(\alpha)\right)\end{aligned} \tag{40}$$

where $\mathrm{SWD(h)}_{\mathrm{aniso}}$ is the anisotropic component of the SWD of the side-crossing signal inside the tomographic region, $\mathrm{SWD}(h_{\mathrm{top}})_{\mathrm{aniso}}$ is the whole anisotropic component of the SWD at the site location, $\lambda_{\mathrm{aniso}}(h)$ is the anisotropic scale factor at the height h, $G_{\mathrm{NS}}^{h_{\mathrm{top}}}$ and $G_{\mathrm{EW}}^{h_{\mathrm{top}}}$ are whole horizontal gradient components in north-south and east-west directions, h_{top} is the height of the tropopause, which is also the same as the top of the tomographic region. h is the height of the side-crossing signal crossing from the tomographic region, and ε and α are the elevation and azimuth angle of the signal (PR), respectively.

C. New Tropospheric Tomographic Equation Matrix

Fig. 5 shows the flowchart of the new tropospheric tomographic model using top-crossed and side-crossed signals.

A whole SWD can be divided into the isotropic and anisotropic components in (1). Therefore, for a side-crossing signal, the SWD inside the tomographic model ($\mathrm{SWD}(h)$) can be estimated using the isotropic and anisotropic scale factors at the height at which the side-crossing signal crosses from the tomographic model. The isotropic and anisotropic scale factors can be obtained by the isotropic scale factor model (BP-ANN model) and (38), respectively. Then, this $\mathrm{SWD}(h)$

can be expressed by merging (27) and (40)

$$\begin{aligned}&\mathrm{SWD}\,(h)\\&\quad=\lambda_{\mathrm{iso}}\,(h)\;mf_w\,(\varepsilon)\;\mathrm{ZWD}\\&\qquad+\lambda_{\mathrm{aniso}}\,(h)\;mf_g\,(\varepsilon)\;\left(G_{\mathrm{NS}}^{h_{\mathrm{top}}}\;\cos(\alpha)+G_{\mathrm{EW}}^{h_{\mathrm{top}}}\sin(\alpha)\right).\end{aligned}\tag{41}$$

$\mathrm{SWD}(h)$ can be transformed into $\mathrm{SWV}(h)$ using (2). The observation equations for the side-crossing signals in the matrix form are as follows:

$$\boldsymbol{SWV_{side}}=\boldsymbol{A_{side}X}\tag{42}$$

where $\boldsymbol{SWV_{side}}$ is the observation vectors from the side-crossing signals, $\boldsymbol{A_{side}}$ is the observation matrix of side-crossing signals, and $\boldsymbol{X}$ is the same as that in (6).

Therefore, the new tropospheric tomographic equation system can be expressed as follows:

$$\begin{pmatrix}\boldsymbol{P_{top}SWV_{top}}\\ \boldsymbol{P_{side}SWV_{side}}\\ 0\\ 0\end{pmatrix}=\begin{pmatrix}\boldsymbol{P_{top}A_{top}}\\ \boldsymbol{P_{side}A_{side}}\\ \boldsymbol{P_{hz}H}\\ \boldsymbol{P_{vr}V}\end{pmatrix}\boldsymbol{X}\tag{43}$$

where $\boldsymbol{SWV_{top}}$ and $\boldsymbol{SWV_{side}}$ denote the observation vectors from the top and side-crossing signals, respectively, $\boldsymbol{A_{top}}$ and $\boldsymbol{A_{side}}$ are the observation matrices of the top and side-crossing signals, respectively, $\boldsymbol{P_{top}}$, $\boldsymbol{P_{side}}$ $\boldsymbol{P_{hr}}$, $\boldsymbol{P_{vr}}$ denote the weight matrices of observation equations for top-crossing signals, side-crossing signals, horizontal and vertical constraints, respectively, and $\boldsymbol{X}$ denotes the vector of the unknown WVD parameters of all voxels in the tomographic region.

IV. Evaluation of the Improved Tropospheric Tomographic Model

A. Evaluation of the Isotropic Scale Factor Model

In this section, the result of $\lambda_{\mathrm{iso}}(h)$ from the new model are evaluated using radiosonde and ERA5 grid data in the year 2020 as the references. To exhibit the effect of the new model, the isotropic scale factor of the HFM is compared. In Zhang et al. [29], the exponential law defined in (44) is adopted to fit the isotropic scale factor model based on 30-year radiosonde data, and its formula is as follows:

$$\lambda_{\mathrm{iso}}^{\mathrm{exp}}(h)=a_1e^{b_1h}+a_2e^{b_2h}\tag{44}$$

where $\lambda_{\mathrm{iso}}^{\mathrm{exp}}(h)$ is the isotropic scale factor from the HFM, a_1, a_2, b_1 and b_2 are the fitting coefficients estimated by the least-squares method, and h is the height of the signal crossing from the tomographic model.

The exponential model and the new model are called ISFEXP and ISFBP, respectively, in this study. In Table I, the monthly fitting results of the ISFEXP based on radiosonde data of each month during the 20 years of 2000–2019 are listed. The last column of the table denotes the residual of the fitting model. The 12 residuals are in the range from 0.036 (August) to 0.083 (December) with a mean value of 0.055.

TABLE I
Monthly $\lambda_{\mathrm{iso}}^{\mathrm{EXP}}(h)$ Fitting Result of ISFEXP (Exponential Model) Based on Radiosonde Data of Each Month During the 20 Years (2000–2019)

Month	a1	b1	a2	b2	Residual
1	1.090	−0.009	−1.176	−0.511	0.077
2	1.129	−0.012	−1.220	−0.498	0.067
3	1.167	−0.015	−1.235	−0.425	0.060
4	1.131	−0.011	−1.185	−0.407	0.048
5	1.102	−0.008	−1.140	−0.385	0.045
6	1.100	−0.007	−1.132	−0.373	0.039
7	1.063	−0.005	−1.098	−0.409	0.038
8	1.084	−0.006	−1.121	−0.389	0.036
9	1.128	−0.010	−1.172	−0.387	0.042
10	1.102	−0.008	−1.143	−0.416	0.057
11	1.081	−0.007	−1.135	−0.456	0.066
12	1.106	−0.010	−1.177	−0.468	0.083

TABLE II
Statistical Results of Fig. 6

Statistical results	Bias		RMSE		STD	
	ISFEXP	ISFBP	ISFEXP	ISFBP	ISFEXP	ISFBP
Mean	0.0002	−0.0046	0.0497	0.0439	0.0486	0.0422

1) Validation With Isotropic Scale Factor Derived From Radiosonde Data: The $\lambda_{\mathrm{iso}}(h)$−ISFEXP (the exponential model) and $\lambda_{\mathrm{iso}}(h)$−ISFBP (the new model) at the position of the radiosonde station for the year 2020 are calculated and the predicted results from the two models are compared with the monthly radiosonde result called $\lambda_{\mathrm{iso}}(h)-\mathrm{RS}$. Their (a) bias, (b) RMSE, and (c) STD of the ISFBP and ISFEXP models are shown in Fig. 6.

Fig. 6(a) indicates that the 8 monthly biases of $\lambda_{\mathrm{iso}}(h)-$ −ISFEXP (blue) are smaller than that of $\lambda_{\mathrm{iso}}(h)-\mathrm{ISFBP}$. The mean of bias values of $\lambda_{\mathrm{iso}}(h)-\mathrm{ISFEXP}$ is closer to zero, meaning that the ISFEXP result reflects the general variation trend of $\lambda_{\mathrm{iso}}(h)$. The biases of nine months from the ISFBP are negative, meaning that the ISFBP underestimates $\lambda_{\mathrm{iso}}(h)$ when radiosonde data are used as the reference. The means of all the monthly results shown in Fig. 4 are listed in Table II. It is noted that the mean bias of $\lambda_{\mathrm{iso}}(h)$−ISFEXP is smaller than that of $\lambda_{\mathrm{iso}}(h)$−ISFBP using the radiosonde data as the reference. This can be because the ISFEXP model is fitted from 20-year radiosonde data and reflects the general variation trend of the scale factor. However, $\lambda_{\mathrm{iso}}(h)$−ISFBP is based on the sample of ERA5 hourly grid data during the 9 years of 2011–2019.

In Fig. 6(b) and (c), all the monthly RMSEs and STDs of the ISFBP results, except for January and April, are smaller than ISFEXP, and the statistical results are shown in Table II. The mean of the RMSEs from ISFEXP and ISFBP are 0.050 and 0.044, respectively. The percentages of the reduction in the RMSE made by ISFBP over ISFEXP is 14%. This implies that, in terms of RMSE, $\lambda_{\mathrm{iso}}(h)$−ISFBP outperforms $\lambda_{\mathrm{iso}}(h)$−ISFEXP. In addition, the two models have smaller RMSEs in the summer than in the winter, probably due to the larger concentration of water vapor in the summer.

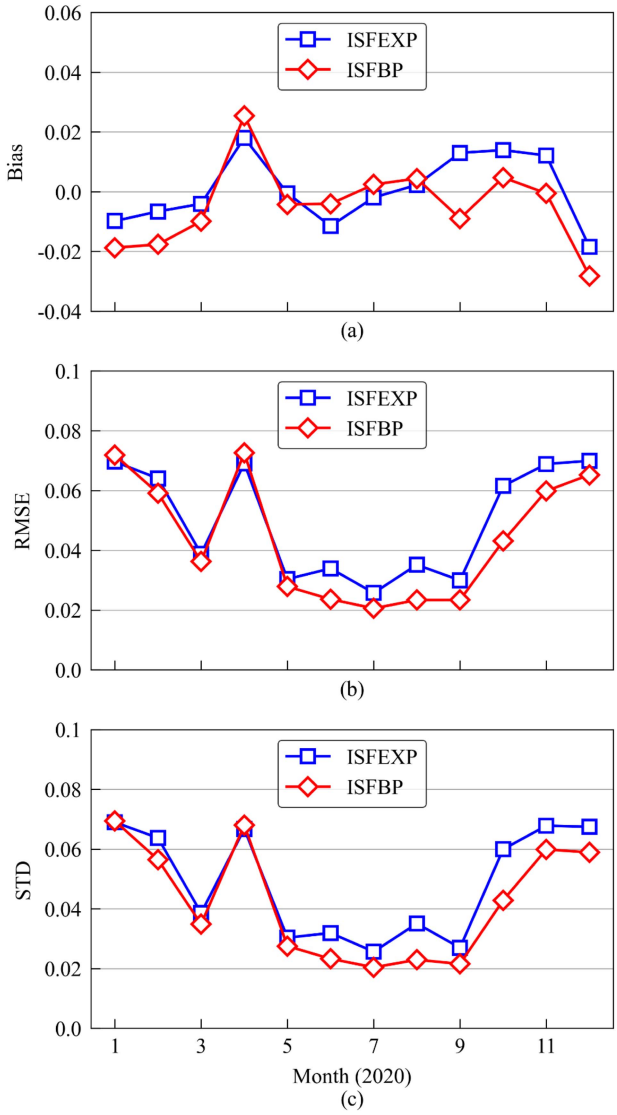

Fig. 6. (a) Monthly bias, (b) RMSE, and (c) STD of the ISFBP (red) model and the ISFEXP (blue) model in 2020 over the position of the radiosonde station. Radiosonde data are used as the reference.

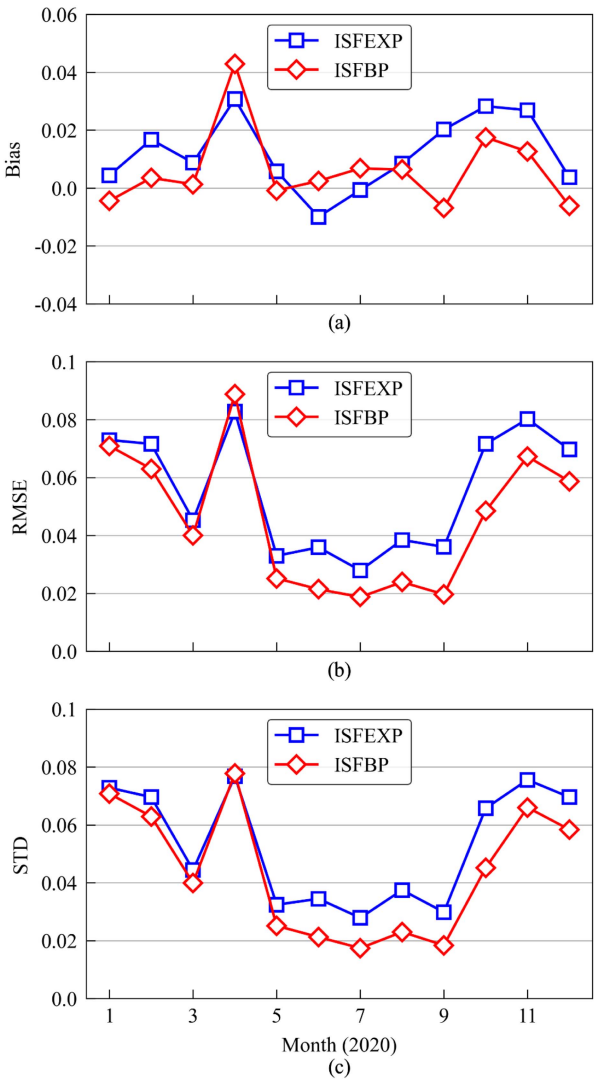

Fig. 7. (a) Monthly mean of the biases, (b) RMSEs, and (c) STDs of ISFBP (red) and ISFEXP (blue) models in 2020. ERA5 data are used as the reference.

TABLE III
STATISTICAL RESULTS OF FIG. 7

Statistical results	Bias		RMSE		STD	
	ISFEXP	ISFBP	ISFEXP	ISFBP	ISFEXP	ISFBP
Mean	0.012	0.006	0.056	0.045	0.053	0.044

2) Validation With Isotropic Scale Factor Derived From ERA5 Data: Since only one radiosonde station is deployed in Hong Kong, the isotropic scale factor only in the location near the radiosonde station (the so-called co-location) can be validated when radiosonde data are used as the reference. If ERA5 grid data are used as the reference, all grid points in the region can be used for the validation. In this section, data from 12 ERA5 grid points in the Hong Kong region in the year 2020 are adopted as the reference to evaluate the above two selected models.

Fig. 7 shows the monthly statistical results of all 12 grid points. For two models, nine monthly biases of isotropic scale factors are positive. Therefore, the two isotropic scale factor models overestimate the isotropic scale factor when ERA5 data are used as the reference. The nine monthly biases of ISFBP are closer to zero than that of ISFEXP. In Table III, which is the statistics of the results shown in Fig. 7, the mean of the 12 monthly biases from ISFBP and ISFEXP are 0.006 and 0.012, respectively, i.e., ISFBP is better in terms of the bias.

From Fig. 7(b) and (c), except for April, all the rest months' RMSEs and STDs from ISFBP are smaller than that of ISFEXP. The maximum percentage of improvement in the RMSE made by ISFBP over ISFEXP is 46% in September, and the minimum value is 3% in January. The number of months with the improvement percentage above 20% is six, and the number of months with the improvement percentage above 10% is 10. However, the improvement percentage is −7.30% in April. The

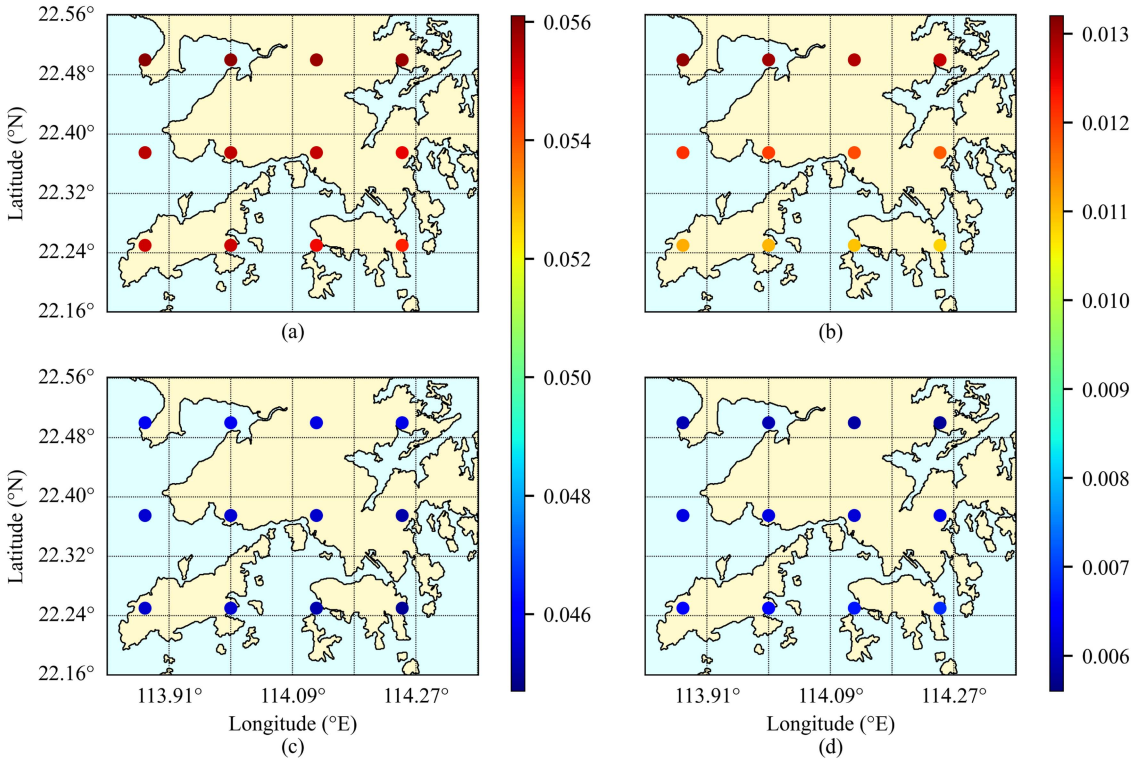

Fig. 8. (a) Mean of 12 monthly RMSEs and (b) biases of ISFEXP (upper), and (c) RMSEs and (d) biases of ISFBP (bottom) in 2020 at 12 ERA5 grid points. ERA5 grid data are used as the reference.

reason may be that the fluctuation of the scale factor in April is larger than that of the other months. In Table III, the mean of all the 12 monthly RMSEs of the ISFBP and ISFEXP are 0.045 and 0.055, respectively, and the mean of the improvement percentages is 22% made by ISFBP over ISFEXP.

To investigate the difference in the RMSEs and biases from the same model but from different grid points, or from the same grid point but from different models, the means of the 12 monthly RMSEs (the left column) and biases (the right column) at 12 grid points from ISFEXP (the upper row) and ISFBP (the bottom row) are shown in Fig. 8.

In the two subfigures (a) and (c) for the RMSE results, the former (ISFEXP) increases with the increase in latitude. The latter (ISFBP) varies little at all the 12 grid points, and the results of the 12 grid points are all considerably smaller than that of the former. Hence, in terms of accuracy, ISFBP outperforms ISFEXP. Similar results are also shown in the two subfigures in the right column for the bias results. Therefore, compared with the model that is based on the sample data from only one radiosonde station, the main advantage of using ERA5 grid data to develop the $\lambda_{\text{iso}}(h)$ model is a better spatial resolution.

B. Tomographic Experiment and Data-Processing Strategy

In this section, experimental results for the improved tropospheric tomographic model, the HFM, and the traditional model are compared. The radiosonde data (only the two epochs at 00:00 and 12:00 UTC each day are available) from the radiosonde station in Hong Kong and ERA5 grid data (with the horizontal resolution of 0.125 × 0.125) are used as two references.

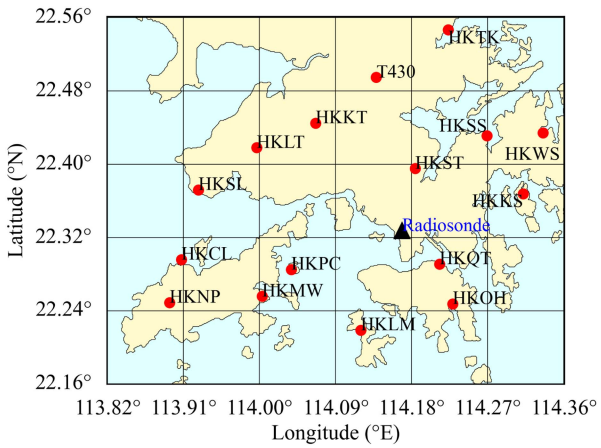

Fig. 9. Distribution of 16 GNSS stations (red dots) and the radiosonde station (black triangle) in Hong Kong.

GNSS data (with a 30s sampling rate) from 16 GNSS stations in the Hong Kong Satellite Positioning Reference Station Network and three IGS stations (BJFS, JFNG, and PIMO) during the 21 days from 1 to 21 August 2019 are selected as the sample data of the tomographic modelling for Hong Kong. Fig. 9 illustrates the spatial distribution of the 16 GNSS stations and the radiosonde station. To adapt to the above mentioned two epochs of radiosonde data, the ERA5 grid data at the same epochs on

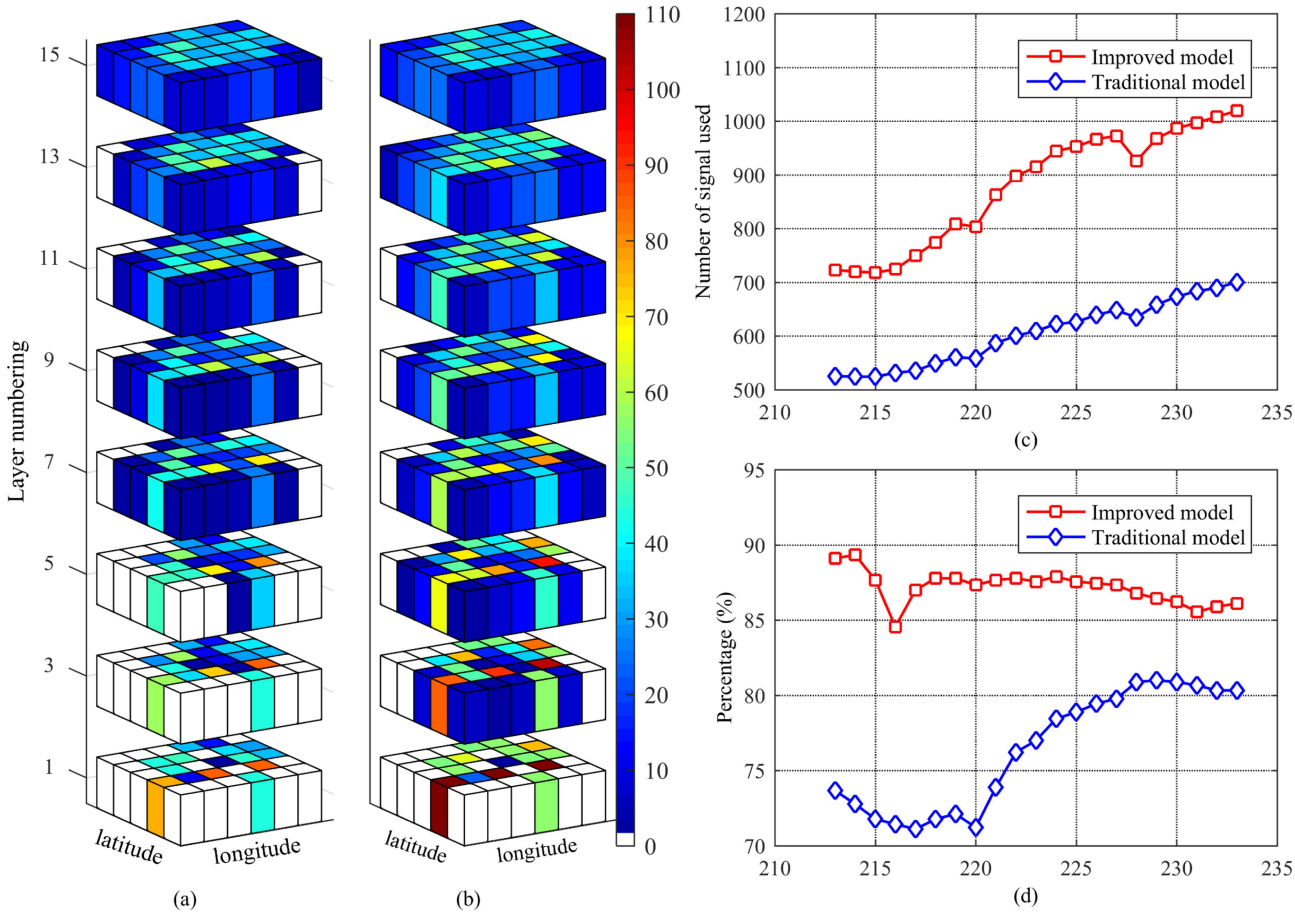

Fig. 10. 3-D distribution of the mean number of signals crossing the tomographic voxels for the (a) traditional and (b) improved tomographic models, where white voxels indicate none-signal-crossing voxels by signals. (c) Shows the mean of the numbers of the signals utilized in the traditional (blue) and the improved (red) model. (d) Shows the mean of the percentages of the voxels crossed by signal rays utilized in the above two models on each day of the 21-day period 1–21 August 2019.

each of the days are retrieved. The tomographic region is divided a certain number of voxels and the number is $5 \times 6 \times 15$. For the horizontal region, the latitude ranges from 22.16° to 22.56°N (with the resolution of 0.08° i.e., 8.88 km) and the longitude ranges from 113.82° to 114.36°E (with the resolution of 0.09° i.e., 9.25 km). The vertical height range is 0–11 km with the resolutions of 1–10 layers (0.4 km), 11–12 layers (1 km), 13–14 layers (1.5 km), and the top layer (2 km).

Since the water vapor content over a site varies slowly within a certain period [45], a 30-min is selected for the tomographic time window in this study, i.e., the temporal resolution of the tomographic reconstruction is 30 min.

The GAMIT/GLOBK (v.10.7) software package and the following strategies are used for the GNSS data processing. The ZTD and delay gradient are estimated with intervals of 0.5 and 2 h, and the ZTD is interpolated to 5 min by the piecewise linear interpolation. The ZHD is calculated by the Saastamoinen model [46], with the input of surface pressure measurements. Equation (1) is used to calculate the SWD. The VMF1 model is selected to calculate the $mf_w(\varepsilon)$. The $mf_g(\varepsilon)$ used in [47] is adopted. The SWD is transformed into the SWV by the conversion factor from (2).

C. Evaluation of Improved Tomographic Model

To evaluate the tomographic results, the number of the signals utilized and the residual of the reconstructed SWVs during the 21 days studied are used. For a comparative analysis, the traditional model which utilizes only those signals crossing from the top boundary of the tomographic region is also evaluated. Fig. 10 shows the 3-D distributions of the mean number of signals crossing the tomographic voxels for the traditional tropospheric tomographic model (a) and the improved tropospheric tomographic model (b), where white voxels indicate none-signal-crossing voxels. (c) shows the daily mean of the numbers of the signals used in the tomographic experiment and (d) shows the daily mean of the percentages of the voxels that are crossed by at least one signal ray. In the two subfigures (a) and (b), the number of empty voxels from the improved model is less than that of the traditional model at most vertical height layers, but the number of the empty voxels at the lowest height layer from two models is the same. This can be because the signals with the elevation angle under 15° are discarded. Therefore, it is difficult for the voxels in the lowest height layer to be crossed by the signal from the station which is in the other voxels at the same height layer.

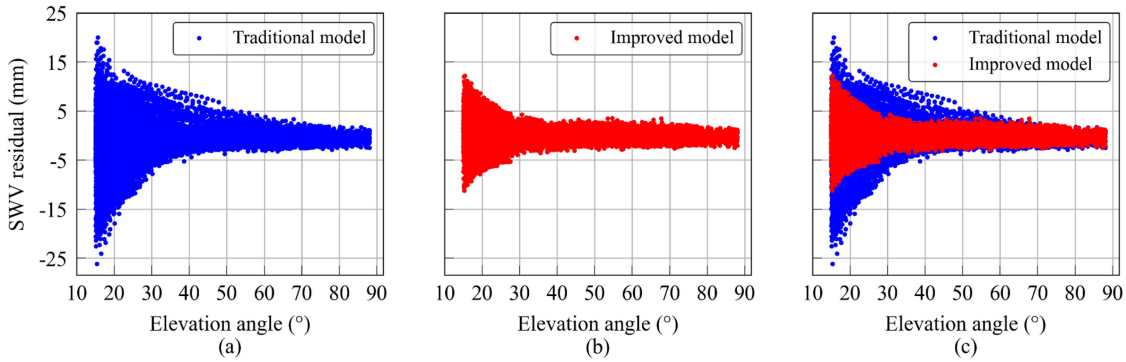

Fig. 11. Variation in the residual of the tomographic model result with elevation angle from the traditional model (blue) and improved model (red) at 00:00 UTC and 12:00 UTC during the 21-day period 1–21 August 2019.

It is noted that only the data that are within the two 30-min periods of 00:00–00:30 UTC and 12:00–12:30 UTC are used to obtain these daily means for (c) and (d). The daily mean of the numbers of the signals and the percentage of the voxels crossed by signals from the improved model (red) are both larger than that of the traditional model (blue). The means of the 21 daily percentages of the voxels crossed by signals shown in (d) are 87% and 76% from the improved model and the traditional model. The percentage of the voxels crossed by signals from the improved tomographic model represents an improvement of 11% over the traditional tomographic model, which may be beneficial to the rank deficiency of the tomographic equations.

Fig. 11 shows the variation in the residual of the improved model (red) and traditional model (blue) with the elevation angle of the signal. The residual is the difference between the SWV reconstructed from the models and the SWV obtained from the GNSS data processing. The residuals of reconstructed SWVs are in the range between −30 and 25 mm, and the absolute values of the residuals decrease with the increase in the elevation angle.

The residuals of the improved model are smaller than that of the traditional model, especially from low elevation angles, which indicates a better performance of the improved model.

The bias/RMSE of the reconstructed SWVs from the improved and traditional tomographic models are also calculated, and the SWVs at 00:00 and 12:00 UTC estimated from the GAMIT/GLOBK (v.10.7) software are used as the reference. The bias/RMSE of the improved and the traditional models are 0.009/1.345 and −0.573/2.852 mm, respectively, which is equivalent to a 53% reduction in the RMSE made by the improved model over the traditional model.

D. Evaluation of Improved Tomographic Model Using Radiosonde Data as Reference

For comparative analyses, three tomographic models including the improved model proposed in this study, the HFM [29], and the traditional model are tested, and their descriptions are shown in Table IV. The radiosonde data from radiosonde station 45004 (located at King's Park, Hong Kong) (see Fig. 9) during the 21 days studied are used as the reference for the three models' results. Fig. 12 shows the tomographic results, i.e., WVD profiles derived from the three tomographic models and the radiosonde data at 12:00 UTC on DOY 230 (rainy day, left pane) and DOY 220 (rainless day, right pane) in 2019. This figure only shows the results of two selected days for an illustration of WVD profiles.

TABLE IV
THREE TOMOGRAPHIC MODELS AND THE SIDE-CROSSING SIGNALS UTILIZED IN THESE MODELS

Model	Where to use side-crossing signals
Traditional model	None
HFM	isotropic component from exponential model + anisotropic component from empirical model
Improved model	isotropic component from BP-ANN model + anisotropic component from empirical model

In Fig. 12(a)–(c) and (e)–(g), the 3-D water vapor fields at 12:00 UTC on DOY 230 (rainy day) and DOY 220 (rainless day) in 2019 are presented. The values of WVD from the improved model are smaller than that of the traditional and HFM models in the low layers from 1 to 3 layers. In the two subfigures (d) and (h), the WVD profiles from the three models are all close to the reference profiles calculated by (4) (blue), but the profiles from the improved model (red) are the closest, especially at the low layers (under 1 km) and high layers (above 4 km), roughly. In addition, the RMSE of the WVD profiles from the improved, HFM and traditional models on the selected two days are also calculated and the results are 1.50/0.89, 1.66/1.91, and 2.08/2.10 g/m^3, respectively, which gives the numerical improvement made by the improved model over the other two models.

Fig. 13 shows the RMSE of the WVDs from three tomographic models at 42 tomographic epochs using radiosonde data as the reference. For 35 tomographic epochs, the RMESs of the tomographic results made by the improved tomographic model are better than that of the traditional tomographic model. The RMSEs of tomographic results from the improved tomographic model are better than that of the HMF at 29 tomographic epochs.

The mean RMESs of 42 tomographic epochs are 1.64, 1.51, and 1.38g/m^3 for the traditional, HFM, and improved tomographic models, respectively.

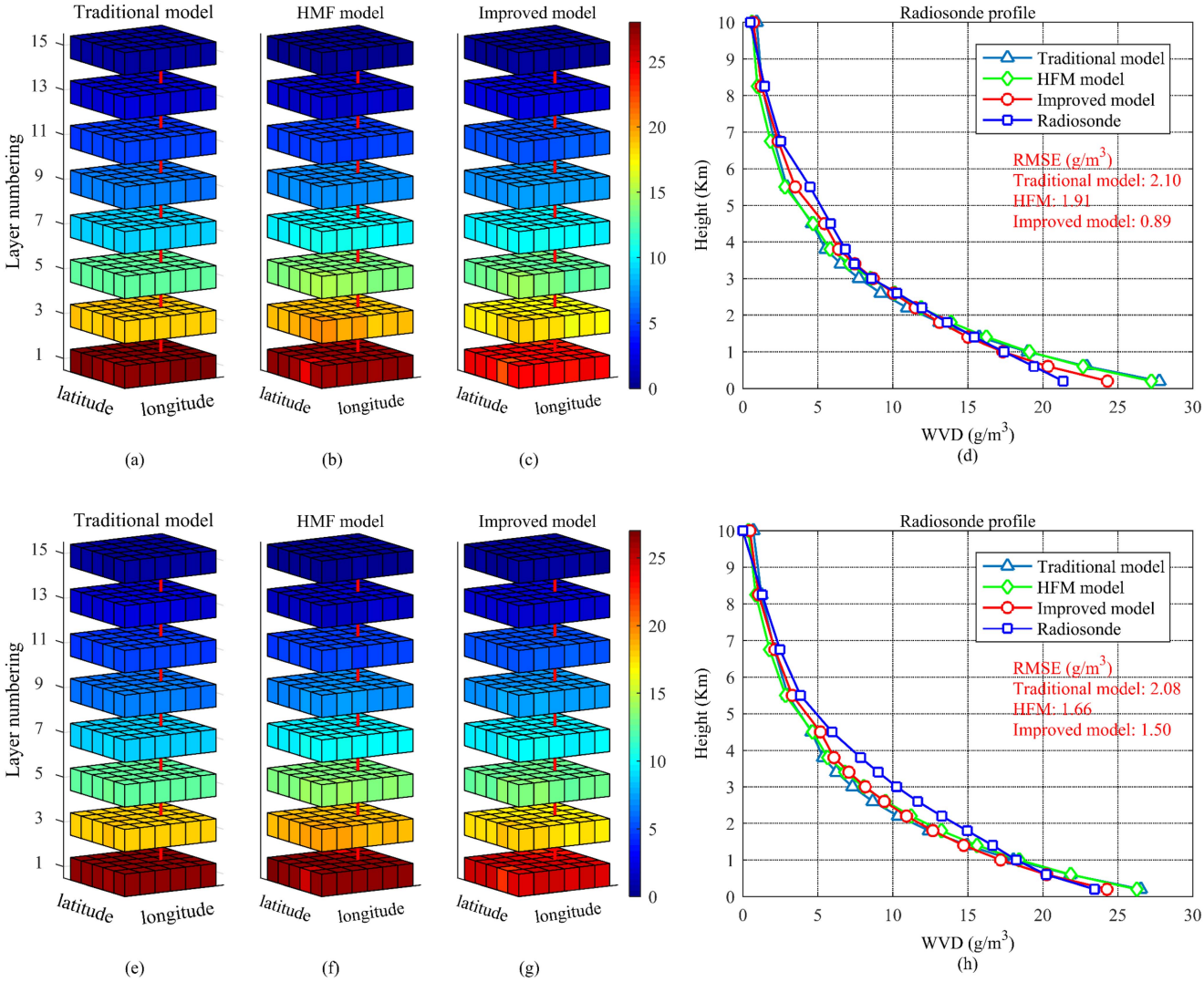

Fig. 12. 3-D water vapour distribution and comparison between WVD profiles resulting from three models against the ones obtained from radiosonde data at 12:00 UTC on DOY 230 (rainy day, top) and DOY 220 (rainless day, bottom) in 2019. (a)–(c) Are the 3-D water vapour distributions of the traditional, HFM, and improved models, respectively. (d) Is the water vapour profile from three models and radiosonde data on the rainy day (top). (e)–(g) Are the 3-D water vapour distributions of three models and (h) is the water vapour profile from three models and radiosonde data on the rainless day (bottom). The red lines denote the location of the voxels including the radiosonde profile.

TABLE V
STATISTICAL RESULTS OF FIG. 13 FOR EACH MODEL

Data	Mean Bias	Mean Mae	Mean RMSE	Non-rainy RMSE	Rainy RMSE
Traditional model−RS	−0.31	1.30	1.64	1.83	1.49
HFM−RS	−0.17	1.18	1.51	1.65	1.40
Improved model−RS	−0.28	1.10	1.38	1.61	1.19

This means that the improved model outperforms the other two models, and the HFM outperforms the traditional model using the radiosonde data as the reference.

Similar to the RMSE shown in Fig. 13, the other two statistical results including Mae and bias are also calculated in Table V. The mean percentages of the reduction in the RMSE made by the improved model over the traditional and HFM models are 16% and 9%, respectively. In addition, the mean Mae of the WVD from the improved model is better than the other two models. However, the mean bias of the HFM is less than that of the improved model. It may be because the HFM is constructed based on the radiosonde data, which is also the reference of the model results. To further study the stability of the new tomographic model under different weather conditions, the mean RMSE of the WVD under nonrainy (9 days) and rainy (12 days) conditions are also shown in Table V. The statistical results show that the new tomographic model has obvious improvement in RMSE than the traditional and HMF models under both nonrainy (9 days) and rainy (12 days) conditions, and the improvement in the rainy days is better than that of the nonrainy days.

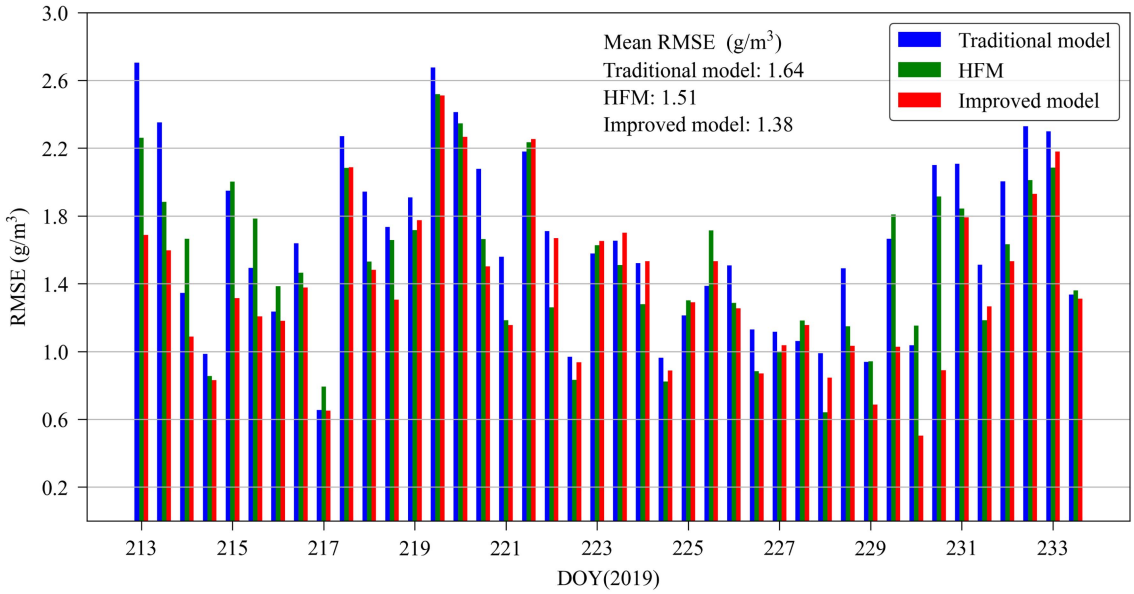

Fig. 13. RMSEs of WVD profiles resulting from three models at 00:00 and 12:00 UTC on each of the 21 days studied. The WVDs from radiosonde data are used as the reference.

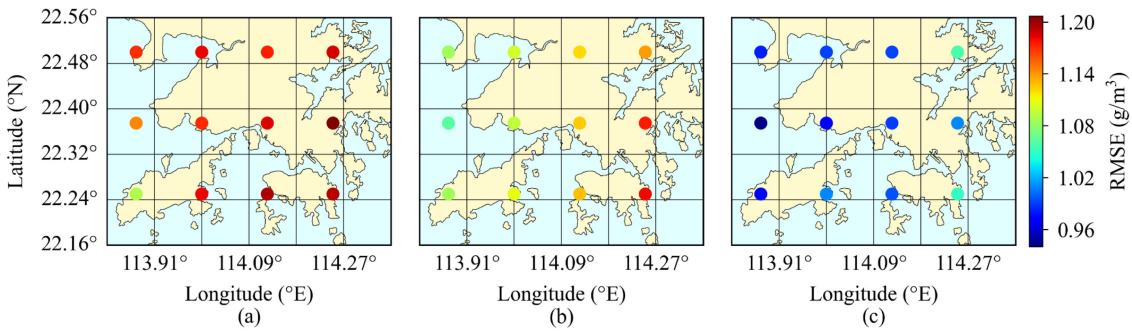

Fig. 14. Mean RMSEs of the WVD profiles for all the tomographic epochs during the 21 days from the (a) traditional model, (b) the HFM, and (c) the improved model at 12 ERA5 grid points using ERA5 grid data as the reference.

E. Evaluation of Improved Tomographic Model Using ERA5 Data as Reference

In this section, the WVDs calculated by (4) from ERA5 grid data (horizontal resolution of 0.125 × 0.125) at 0:00 and 12:00 UTC on the 21 days studied are used as the reference for the evaluation of the three tomographic models. The mean RMSEs of the WVD profiles at all tomographic epochs at 12 grid points are shown in Fig. 14, where the three subfigures (a), (b), and (c) are the results of the traditional model, the HFM, and the improved model, respectively. The RMSEs in each subfigure increase with the increase of longitude. For the comparison among the three subfigures, the RMSEs at all the 12 grid points in (c), i.e., the improved tomographic model, are significantly better than the other two models. This result is similar to the case when radiosonde data are used as the reference.

Fig. 15 shows the mean RMSEs of the 12 grid points on each tomographic epoch from three models. For 34 tomographic epochs, the mean RMESs of the 12 grid points made by the improved tomographic model are better than that of the traditional tomographic model. The mean RMSEs of 12 grid points from the improved tomographic model are better than that of the HMF at 28 tomographic epochs. The mean RMESs of 42 tomographic epochs are 1.31, 1.22, and 1.03 g/m^3 for the traditional, HFM, and improved tomographic models, respectively. The three values indicate that the overall accuracy of the improved model significantly outperforms the other two models, and the HFM slightly outperforms the traditional model.

Similar to the RMSE shown in Fig. 15, the other two statistical results including Mae and bias are also calculated in Table VI. The mean percentages of the reduction in the RMSE made by the improved model over the traditional and HFM models are 22% and 16%, respectively. In addition, the mean Mae of the WVDs from the improved model is better (smaller) than the other two models. However, the mean bias of the HFM (−0.08) is less than that of the improved model (−0.18), meaning that both the models underestimate the WVD, and

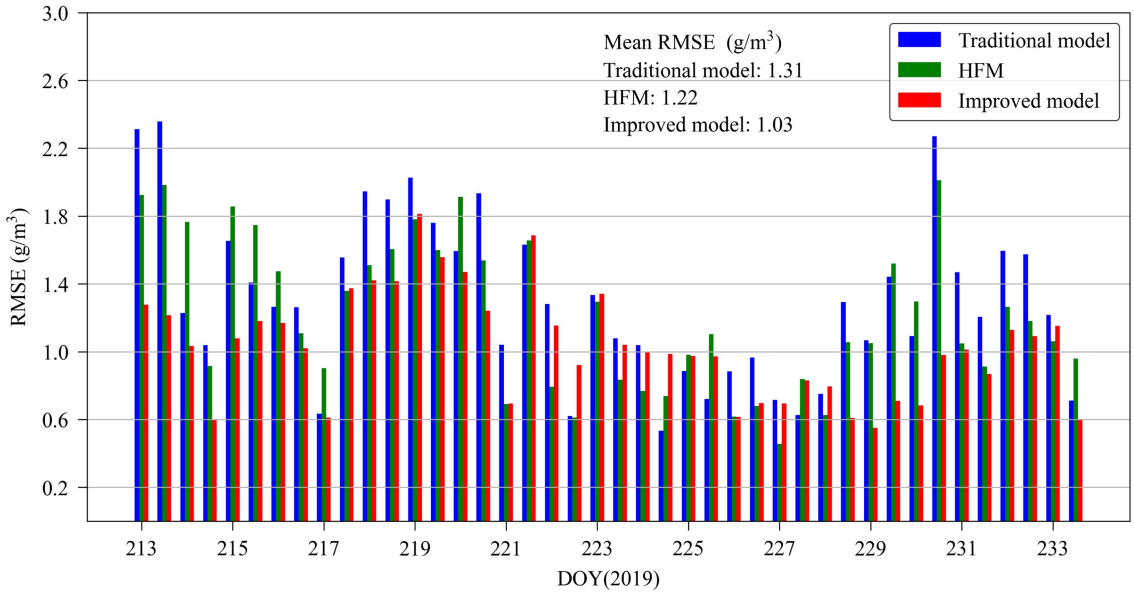

Fig. 15. Mean RMSEs of WVD profiles of 12 grid points on each tomographic epoch resulting from 3 models. The WVDs from ERA5 grid data are used as the reference.

TABLE VI
STATISTICAL RESULTS OF FIG. 15 FOR EACH MODEL

Data	Mean Bias	Mean Mae	Mean RMSE	Non-rainy RMSE	Rainy RMSE
Traditional model−RS	−0.23	1.02	1.31	1.42	1.22
HFM−RS	−0.08	0.93	1.22	1.28	1.17
Improved model−RS	−0.18	0.81	1.03	1.20	0.91

the improved model is worse. The reasons are discussed in the previous section (radiosonde data as the reference) When ERA5 data are used as the reference, the new tomographic model still outperforms the HFM and traditional models under both rainy and nonrainy conditions, and the new model has greater improvement in the rainy days than that of the non-rainy days. The results are similar to the results using radiosonde data as the reference. These results mean that the new tomographic model is more suitable for the tomography of large water vapor variation.

To investigate the relationship between the RMSEs of each model results with altitude, the mean RMSEs of the WVDs at each height layer are calculated and the results are shown in Fig. 16. The results of the improved tomographic model (red) at most height layers are smaller than that of the other two models, especially at the layer that is closest to the surface. This means the improved model performs best at the lowest height layer. Moreover, at low-to-middle layers, i.e., from 1.8 to 3.4 km, roughly, the HFM and the improved model results are similar, and they are much better than the traditional model. At high altitude layers, i.e., above 3.4 km, roughly, the improved model slightly outperforms the other two models.

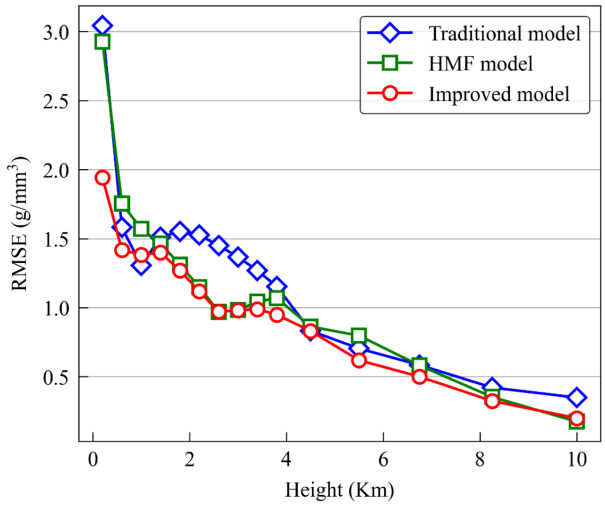

Fig. 16. Mean RMSEs of the WVDs in each height layer from three models. The WVDs from ERA5 data are used as the reference.

V. CONCLUSION

The traditional tropospheric tomographic model only uses the GNSS signals crossing from the top boundary of the tomographic region of interest, while the GNSS signals crossing from the four side faces of the tomographic region are not considered. This leads to a waste of side-crossing signals and a decrease in the number of voxels that are penetrated by these signals. In this study, an improved tropospheric tomographic method based on an artificial neural network is developed using the signals not only crossing from the top boundary of the tomographic region but also crossing from the four side faces of the tomographic region.

The accuracies of the isotropic scale factor from the improved tomographic model and that of the HFM model (both models use side-crossing signals) are compared using two references from radiosonde and ERA5 data. The statistical results show that the mean percentages of the reduction in the RMSE made by the improved model over the HFM are 14% and 22% using radiosonde and ERA5 data as the references, respectively. This suggests that the isotropic scale factor from the improved tropospheric tomographic model is better than that of the HFM. Moreover, the scale factor of the anisotropic component is estimated under the assumption that the variation in the refractivity gradient in the vertical direction is an exponential function of altitude.

To evaluate the improved tropospheric tomographic model, GNSS data from 16 GNSS stations in Hong Kong during the 21 days from 1 to 21 August 2019 are adopted to obtain the tomographic results, and the radiosonde and ERA5 data in the same region and time are used as the references. For the improved tropospheric tomographic model, the mean of the utilization percentages of voxels increases from 76% of the traditional model to 87% of the improved model. The percentage of the reduction in the RMSE of the reconstructed SWVs made by the improved model over the traditional model is 53%. The statistical results of the WVD profiles show that the mean percentages of the reduction in the RMSE made by the improved model over the traditional/HFM models are 16%/9% and 22%/16% using radiosonde and ERA5 data as the references, respectively. Similarly, the comparison of the RMSEs of the WVD profiles at 16 vertical height layers between the three models also shows the superiority of the improved model. Especially, the accuracy of the improved tomographic model has obvious improvement over the HMF and the traditional tomographic model in the lower height layer. These results suggest that the tomographic results from the improved tomographic model are more accurate than that from the other two models.

Our future work will be mainly on utilizing more water vapor data from various technologies, e.g., multi-GNSS, GNSS-R, InSAR and virtual signals from numerical weather prediction models into the tropospheric tomographic system for more refined or better tomographic results.

ACKNOWLEDGMENT

The authors would like to thank the anonymous reviewers for their valuable comments on this article. The authors would also like to thank the Integrated Global Radiosonde Archive (IGRA) and ECMWF for providing access to the web-based IGAR and layered meteorological data. The Lands Department of HKSAR and Hong Kong Observatory is also acknowledged for providing GPS data from the Hong Kong Satellite Positioning Reference Station Network (SatRef) and weather information, respectively.

REFERENCES

[1] G. Guerova et al., "Review of the state of the art and future prospects of the ground-based GNSS meteorology in Europe," *Atmospheric Meas. Techn.*, vol. 9, no. 11, pp. 5385–5406, Jun. 2016, doi: 10.5194/amt-9-5385-2016.

[2] X. Wang et al., "The correlation between GNSS-derived precipitable water vapor and sea surface temperature and its responses to El Niño–Southern oscillation," *Remote Sens. Environ.*, vol. 216, pp. 1–12, Oct. 2018, doi: 10.1016/j.rse.2018.06.029.

[3] N. Hanna, E. Trzcina, G. Möller, W. Rohm, and R. Weber, "Assimilation of GNSS tomography products into the weather research and forecasting model using radio occultation data assimilation operator," *Atmospheric Meas. Techn.*, vol. 12, no. 9, pp. 4829–4848, Sep. 2019, doi: 10.5194/amt-12-4829-2019.

[4] H. Li et al., "A new cumulative anomaly-based model for the detection of heavy precipitation using GNSS-derived tropospheric products," *IEEE Trans. Geosci. Remote Sens.*, vol. 60, 2022, Art. no. 4105718.

[5] Q. Zhao, Y. Liu, W. Yao, and Y. Yao, "Hourly rainfall forecast model using supervised learning algorithm," *IEEE Trans. Geosci. Remote Sens.*, vol. 60, 2022, Art. no. 4100509.

[6] A. Flores, G. Ruffini, and A. Rius, "4D tropospheric tomography using GPS slant wet delays," *Annales Geophysicae*, vol. 18, no. 2, pp. 223–234, Feb. 2000, doi: 10.1007/s00585-000-0223-7.

[7] K. Hirahara, "Local GPS tropospheric tomography," *Earth Planets Space*, vol. 52, no. 11, pp. 935–939, Aug. 2000, doi: 10.1186/BF03352308.

[8] L. P. Gradinarsky and P. Jarlemark, "Ground-based GPS tomography of water vapor: Analysis of simulated and real data," *J. Meteorological Soc. Jpn.*, vol. 82, no. 1B, pp. 551–560, Mar. 2004, doi: 10.2151/jmsj.2004.551.

[9] M. Bender et al., "Development of a GNSS water vapour tomography system using algebraic reconstruction techniques," *Adv. Space Res.*, vol. 47, no. 10, pp. 1704–1720, May 2011, doi: 10.1016/j.asr.2010.05.034.

[10] M. Heublein, X. X. Zhu, F. Alshawaf, M. Mayer, R. Bamler, and S. Hinz, "Compressive sensing for neutrospheric water vapor tomography using GNSS and InSAR observations," in *Proc. IEEE Int. Geosci. Remote Sens. Symp.*, 2015, pp. 5268–5271, doi: 10.1109/IGARSS.2015.7327023.

[11] F. Yang et al., "A GPS water vapour tomography method based on a genetic algorithm," *Atmospheric Meas. Techn.*, vol. 13, no. 1, pp. 355–371, Jan. 2020, doi: 10.5194/amt-13-355-2020.

[12] S. Song, W. Zhu, J. Ding, and J. Peng, "3D water-vapor tomography with Shanghai GPS network to improve forecasted moisture field," *Chin. Sci. Bull.*, vol. 51, no. 5, pp. 607–614, Mar. 2006, doi: 10.1007/s11434-006-0607-5.

[13] P. Elósegui et al., "Sensing atmospheric structure using small-scale space geodetic networks," *Geophys. Res. Lett.*, vol. 26, no. 16, pp. 2445–2448, Aug. 1999, doi: 10.1029/1999GL900585.

[14] P. Xia, C. Cai, and Z. Liu, "GNSS troposphere tomography based on two-step reconstructions using GPS observations and COSMIC profiles," *Annales Geophysicae*, vol. 31, no. 10, pp. 1805–1815, Oct. 2013, doi: 10.5194/angeo-31-1805-2013.

[15] P. Benevides, J. Catalao, G. Nico, and P. M. A. Miranda, "4D wet refractivity estimation in the atmosphere using GNSS tomography initialized by radiosonde and AIRS measurements: Results from a 1-week intensive campaign," *GPS Solutions*, vol. 22, no. 4, Jul. 2018, Art. no. 91, doi: 10.1007/s10291-018-0755-5.

[16] P. Benevides, G. Nico, J. Catalão, and P. M. A. Miranda, "Bridging InSAR and GPS tomography: A new differential geometrical constraint," *IEEE Trans. Geosci. Remote Sens.*, vol. 54, no. 2, pp. 697–702, Feb. 2016.

[17] M. Heublein, F. Alshawaf, B. Erdnüß, X. Zhu, and S. Hinz, "Compressive sensing reconstruction of 3D wet refractivity based on GNSS and InSAR observations," *J. Geodesy*, vol. 93, no. 2, pp. 197–217, Jun. 2018, doi: 10.1007/s00190-018-1152-0.

[18] P. Benevides, J. Catalao, G. Nico, and P. M. A. Miranda, "Inclusion of high resolution MODIS maps on a 3D tropospheric water vapor GPS tomography model," in *Proc. Conf. Remote Sens. Clouds Atmos. XX*, 2015, vol. 9640, Art. no. 96400R, doi: 10.1117/12.2194857.

[19] W. Zhang, S. Zhang, N. Zheng, N. Ding, and X. Liu, "A new integrated method of GNSS and MODIS measurements for tropospheric water vapor tomography," *GPS Solutions*, vol. 25, no. 2, Mar. 2021, Art. no. 79, doi: 10.1007/s10291-021-01114-1.

[20] W. Zhang, S. Zhang, N. Ding, L. Holden, X. Wang, and N. Zheng, "GNSS-RS tomography: Retrieval of tropospheric water vapor fields using GNSS and RS observations," *IEEE Trans. Geosci. Remote Sens.*, vol. 60, 2022, Art. no. 4102313.

[21] M. Zhang et al., "A new method for tropospheric tomography using GNSS and Fengyun-4A data," *Atmospheric Res.*, vol. 280, Oct. 2022, Art. no. 106460, doi: 10.1016/j.atmosres.2022.106460.

[22] B. Chen and Z. Liu, "Assessing the performance of troposphere tomographic modeling using multi-source water vapor data during Hong Kong's rainy season from May to October 2013," *Atmospheric Meas. Techn.*, vol. 9, no. 10, pp. 5249–5263, Oct. 2016, doi: 10.5194/amt-9-5249-2016.

[23] P. Benevides, G. Nico, J. Catalao, and P. M. A. Miranda, "Analysis of Galileo and GPS integration for GNSS tomography," *IEEE Trans. Geosci. Remote Sens.*, vol. 55, no. 4, pp. 1936–1943, Apr. 2017.
[24] Z. Dong and S. Jin, "3-D water vapor tomography in Wuhan from GPS, BDS and GLONASS observations," *Remote Sens.*, vol. 10, no. 1, pp. 62–76, Jan. 2018, doi: 10.3390/rs10010062.
[25] W. Rohm and J. Bosy, "The verification of GNSS tropospheric tomography model in a mountainous area," *Adv. Space Res.*, vol. 47, no. 10, pp. 1721–1730, May 2011, doi: 10.1016/j.asr.2010.04.017.
[26] Y. Yao, Q. Zhao, and B. Zhang, "A method to improve the utilization of GNSS observation for water vapor tomography," *Annales Geophysicae*, vol. 34, no. 1, pp. 143–152, Jan. 2016, doi: 10.5194/angeo-34-143-2016.
[27] Q. Zhao, Y. Yao, W. Yao, and P. Xia, "An optimal tropospheric tomography approach with the support of an auxiliary area," *Annales Geophysicae*, vol. 36, no. 4, pp. 1037–1046, Jul. 2018, doi: 10.5194/angeo-36-1037-2018.
[28] Q. Zhao, W. Yao, Y. Yao, and X. Li, "An improved GNSS tropospheric tomography method with the GPT2w model," *GPS Solutions*, vol. 24, no. 2, Mar. 2020, Art. no. 60, doi: 10.1007/s10291-020-0974-4.
[29] W. Zhang, S. Zhang, N. Ding, and Q. Zhao, "A tropospheric tomography method with a novel height factor model including two parts: Isotropic and anisotropic height factors," *Remote Sens.*, vol. 12, no. 11, pp. 1848–1870, Jun. 2020, doi: 10.3390/rs12111848.
[30] B. Chen and Z. Liu, "Voxel-optimized regional water vapor tomography and comparison with radiosonde and numerical weather model," *J. Geodesy*, vol. 88, no. 7, pp. 691–703, Apr. 2014, doi: 10.1007/s00190-014-0715-y.
[31] Y. Yao and Q. Zhao, "A novel, optimized approach of voxel division for water vapor tomography," *Meteorol. Atmospheric Phys.*, vol. 129, no. 1, pp. 57–70, Feb. 2017, doi: 10.1007/s00703-016-0450-4.
[32] T. A. Herring, R. W. King, and S. C. Mcclusky, *GPS Analysis at MIT, GAMIT Reference Manual, Release 10.3*. Cambridge, MA, USA: Massachusetts Inst. Technol., 2010.
[33] G. D. Thayer, "An improved equation for the radio refractive index of air," *Radio Sci.*, vol. 9, no. 10, pp. 803–807, Oct. 1974, doi: 10.1029/RS009i010p00803.
[34] Y. Liu, Y. Chen, and J. Liu, "Determination of weighted mean tropospheric temperature using ground meteorological measurements," *Geo-Spatial Inf. Sci.*, vol. 4, no. 1, pp. 14–18, Aug. 2001, doi: 10.1007/BF02826630.
[35] I. Durre, R. S. Vose, and D. B. Wuertz, "Overview of the integrated global radiosonde archive," *J. Climate*, vol. 19, no. 1, pp. 53–68, Jan. 2006, doi: 10.1175/JCLI3594.
[36] J. L. Davis, T. A. Herring, I. I. Shapiro, A. E. E. Rogers, and G. Elgered, "Geodesy by radio interferometry: Effects of atmospheric modeling errors on estimates of baseline length," *Radio Sci.*, vol. 20, no. 6, pp. 1593–1607, Dec. 1985, doi: 10.1029/RS020i006p01593.
[37] Q. Zhao, J. Su, C. Xu, Y. Yao, X. Zhang, and J. Wu, "High-precision ZTD model of altitude-related correction," *IEEE J. Sel. Topics Appl. Earth Observ. Remote Sens.*, vol. 16, pp. 609–621, 2023.
[38] H. Hersbach et al., "ERA5 hourly data on pressure levels from 1979 to present," Copernicus Climate Change Service (C3S) Climate Data Store (CDS), 2018, doi: 10.24381/cds.bd0915c6.
[39] H. Li et al., "A neural network-based approach for the detection of heavy precipitation using GNSS observations and surface meteorological data," *J. Atmospheric Sol.-Terrestrial Phys.*, vol. 225, no. 1, Nov. 2021, Art. no. 105763, doi: 10.1016/j.jastp.2021.105763.
[40] L. Li et al., "A new zenith hydrostatic delay model for real-time retrievals of GNSS-PWV," *Atmospheric Meas. Techn.*, vol. 14, no. 10, pp. 6379–6394, Oct. 2021, doi: 10.5194/amt-14-6379-2021.
[41] X. Ma, Y. Yao, B. Zhang, and C. He, "Retrieval of high spatial resolution precipitable water vapor maps using heterogeneous earth observation data," *Remote Sens. Environ.*, vol. 278, Sep. 2022, Art. no. 113100, doi: 10.1016/j.rse.2022.113100.
[42] J. Li, J. Cheng, J. Shi, and F. Huang, "Brief introduction of back propagation (BP) neural network algorithm and its improvement," in *Advances in Computer Science and Information Engineering*. Berlin, Germany: Springer, 2012, pp. 553–558, doi: 10.1007/978-3-642-30223-7_87.
[43] J. Boehm and H. Schuh, "Troposphere gradients from the ECMWF in VLBI analysis," *J. Geodesy*, vol. 81, nos. 6–8, pp. 403–408, Mar. 2007, doi: 10.1007/s00190-007-0144-2.
[44] D. Landskron and J. Böhm, "Refined discrete and empirical horizontal gradients in VLBI analysis," *J. Geodesy*, vol. 92, no. 12, pp. 1387–1399, Feb. 2018, doi: 10.1007/s00190-018-1127-1.
[45] P. Benevides, J. Catalão, and P. M. A. Miranda, "Experimental GNSS tomography study in Lisbon (Portugal)," *Física de la Tierra*, vol. 26, pp. 65–79, Nov. 2014, doi: 10.5209/rev_FITE.2014.v26.46972.
[46] J. Saastamoinen, "Atmospheric correction for the troposphere and the stratosphere in radio ranging satellites," *Artif. Satellites Geodesy*, vol. 15, pp. 247–251, Jan. 1972, doi: 10.1029/GM015p0247.
[47] G. Chen and T. A. Herring, "Effects of atmospheric azimuthal asymmetry on the analysis of space geodetic data," *J. Geophys. Res., Solid Earth*, vol. 102, no. B9, pp. 20489–20502, Sep. 1997, doi: 10.1029/97JB01739.

Minghao Zhang received the B.Sc. degree in surveying engineering from the China University of Mining and Technology, Xuzhou, China, in 2020. He is currently working toward the Ph.D. degree in geodesy and surveying engineering in the School of Environment Science and Spatial Informatics, China University of Mining and Technology.

His research interests include global navigation satellite system meteorology.

Kefei Zhang received the Ph.D. degree in geodesy from Curtin University, Perth, WA, Australia, in 1998.

He is a Professor with the China University of Mining and Technology, Xuzhou, China, and an honorary Professor with RMIT University, Melbourne, Vic, Australia. His research interests include positioning, navigation and timing, GNSS for weather and climate, geodetic data analytics, extra-terrestrial resources exploration and utilization, space situational awareness, and space weather.

Suqin Wu received the Ph.D. degree in geodesy and surveying engineering from RMIT University, Melbourne, Vic, Australia, in 2009.

She is currently a Professor with the China University of Mining and Technology, Xuzhou, China. Her research interests mainly include GNSS precise positioning and GNSS meteorology, GPS radio occultation, atmospheric error modeling for high accuracy GNSS applications, and precise orbit determination and prediction for space debris objects, etc.

Longjiang Li received the B.Sc. degree in surveying engineering in 2018 from China University of Mining and Technology, Xuzhou, China, where he is currently working toward the Ph.D. degree in geodesy and geomatics engineering.

His current research interests include the retrieval of PWV from GNSS observation and its application in extreme weather forecast.

Dantong Zhu received the Ph.D. degree in geodesy and surveying engineering from the China University of Mining and Technology, Xuzhou, China, in 2022.

He is currently a Lecturer with North China University of Water Resources and Electric Power, Zhengzhou, China. His research interests include global navigation satellite meteorological studies and high-precision data processing.

Moufeng Wan received the Ph.D. degree in geodesy and surveying engineering from the China University of Mining and Technology, Xuzhou, China, in 2023.

His research interests include robust and adaptive nonlinear Kalman filtering and its application in GNSS navigation. His current research interests include GNSS tomography, four-dimensional atmospheric water vapor modelling, meteorological applications of GNSS, and spatial distribution and variation mechanism of small/medium scale tropospheric water vapor.

Peng Sun received the Ph.D. degree in geodesy and surveying engineering from the China University of Mining and Technology (CUMT), Xuzhou, China, in 2022.

He is currently a Postdoctor with CUMT. His current research interests include GNSS precise point positioning and GNSS meteorology.

Jiaqi Shi received the M.S. degree in geodesy and surveying engineering from the School of Environment Science and Spatial Informatics, China University of Mining and Technology, Xuzhou, China, in 2022. He is currently working toward the Ph.D. degree in GNSS Research Center, Wuhan University, Wuhan, China.

His main research interests include radio occultation and GNSS meteorology.

Shangyi Liu received the B.Sc. degree in surveying engineering from the School of Geodesy and Geomatics, Wuhan University, Wuhan, China, in 2020. He is currently working toward the M.S. degree in surveying and mapping engineering in the School of Environment Science and Spatial Informatics, China University of Mining and Technology, Xuzhou, China.

His main research interests include global navigation satellite system meteorology.

Andong Hu received the Ph.D. degree in geospatial science from Royal Melbourne Institute of Technology University, Melbourne, Vic, Australia, in 2020.

He is currently working as a Postdoc with CU Boulder, Boulder, CO, USA, and NOAA Space Weather Prediction Center, Boulder. His current research interests include machine learning algorithm development and innovative applications of space weather modeling for solar wind prediction, solar wind and magnetosphere coupling, and ionosphere analysis.